UNIVERSITY OF OSLO
Department of Physics

Modelling and characterization of electrical properties of ZnO-based heterostructures for solar cell applications

Master thesis

Chi Kwong Tang

1st June 2009

Acknowledgement

I will begin by expressing my greatest gratitude to my supervisors; Edouard Monakhov - for his patience and guidance when I was wandering around confusingly in the wildness of science, Lasse Vines - for the help with all the instruments employed and the great advices to my many obstacles, and Bengt G. Svensson - for introducing me to the field of semiconductor and correcting my many hidden errors in the text. This work would have shaped differently if it was not for the touch of their valuable time, which I appreciate very much.

Moving on to my list comes Knut E. Knutsen and Jonathan Polfus for the many master-meetings and deadlines to discuss the details of the text and its layout. It pleases my eyes to see the same font type every possible places in the text and a minor space before the units. I also appreciate the scientific discussions with Helge Malmbekk and Klaus Magnus Johansen, which showed me some of the other angles of looking at a problem. Thanks to Ramon Schifano for a helpful discussion surrounding palladium Schottky contacts. Thanks to everybody at MiNa-lab for a great time. Thanks to all the participants of the weekly "felleslunsj" who created another special day in a week during the whole master period, to avoid a long list, you all know who you are. Thanks to all my friends for the encouragement and uplifting words during the difficult times like when experiments and simulations fail in every possible ways.

Last but not least, I would like to thank my family for the support and all the delicious dinners when I arrive home hungry and exhausted after a hard working day.

Abstract

Zinc oxide (ZnO) is becoming an attractive semiconductor material within optoelectronics and solar cell applications. The usage of ZnO as a transparent conducting oxide (TCO) is interesting both as electrode in Si-based cells and used in band gap engineered heterojunction solar cells. Device performance can be estimated by charge carrier simulation using commercially available software (TCAD), but a reliable model of the transport properties of ZnO is needed.

In the present study, ZnO-based heterostructure and Schottky contact have been modelled and simulated for their electrical characteristics. The ZnO model was developed and investigated through experimental characterization of Pd Schottky contacts on ZnO using capacitance-voltage (CV), current-voltage (IV), deep level transient spectroscopy (DLTS) and admittance spectroscopy (ADSPEC).

A heterostructure of highly doped n-type ZnO on Si was explored for its potential within solar cell application. In the ideal model, an illumination using single wavelength of 2 eV and a power of 2.9 mW/cm^2 corresponding to AM1.5 was implemented and the highest achieved conversion efficiency was 15.9% on p-type Si substrate.

Contents

Chapter 1

Introduction

Besides the usage of powder zinc oxide (ZnO) in a wide range of commercialized products [1], zinc oxide is gaining an increasing interest as a semiconductor material. Its combination of direct band gap of 3.4 eV and high exciton binding energy of 60 meV opens up the possibility of high efficient solid state illumination [2]. In addition, achievable high electrical conductivity in ZnO enables it to become a transparent conducting oxide comparable to indium tin oxide, which already has many applications today, such as touch panel and front contact on solar cells. The large availability of high quality bulk crystal is an advantage over its competitors, e.g. GaN, where production cost can be reduced. Zinc, being much more abundant than indium, is also beneficial in the increasing demand for transparent conducting oxide.

Before realizing the mentioned usage areas, much fundamental understandings in the electrical properties still remain to be uncovered. The most commonly referred issues met in ZnO-based devices have been the stability and reproducibility of p-type doping and Schottky contacts . Much research has been devoted to p-type thin film ZnO in order to enable a homojunction and fully utilize the potential of ZnO. On the other hand, the well established n-type ZnO is under investigation for heterojunction in optoelectonic applications.

The goal of this thesis is to build a simulation model of the electrical transport properties of ZnO based on the findings in the literature and ex-

perimental characterization, and utilize the model to numerically investigate the potentials of ZnO/Si heterojunction for solar cell applications.

Thesis overview

This thesis will begin by introducing the theoretical background needed to follow the presented work. A brief introduction to ZnO and the relevant literatures are then given to understand the nature of this material. The simulation software and the characterization techniques which are employed will be discussed followed by the developement and discussion of the simulation model of ZnO through Pd Schottky contact. At the end, ZnO/Si heterostructure simulation results are presented and discussed before conclusion and the suggestions for future work.

Chapter 2

Background

This chapter briefly reviews the fundamental knowledge about common semiconductor crystal structures and semiconductor physics that is important to predict the properties of a material.

2.1 Crystallography

2.1.1 Crystal structure

A crystal can be represented by periodically arranging their building block, also called *unit cell*. These cells are grouped into 14 *bravais lattices* which are again categorized in 7 *crystal systems*. Bravais lattices differ from each other by their lattice constants and angles.

Semiconductors often adapt diamond, zinc blende or wurtzite structure which is derived from the Face Centered Cubic (FCC) or Hexagonal Closest Packed (HCP) system (see Fig. 2.1). Diamond and zinc blende are structurally equal, but they separate by having 1 and 2 types of elements in the structure, respectively. By shifting two FCC by a coordinate of $(\frac{1}{4}, \frac{1}{4}, \frac{1}{4})$ relative to each other, these two structures can be constructed.

ZnO adapts the wurtzite structure, and further investigations of the unit cell of wurtzite reveal that its symmetry is non-centrosymmetric. This gives rise to properties such as ferro-, pyro-, piezo- and dielectricity, which are crucial in Micro-Electro-Mechanical-System (MEMS). It is important to

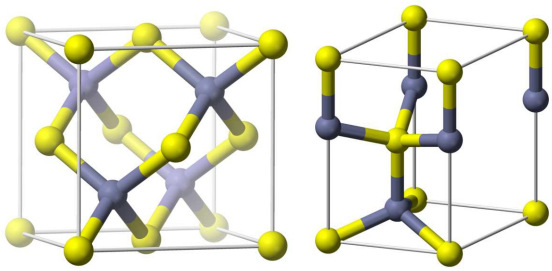

(a) Zinc blende/Diamond (b) Wurtzite

Figure 2.1: The structure of zinc blende and wurtzite. Diamond structure is achieved by regarding the atoms in zinc blende to be of the same type.

realize that a unit cell has properties dependent on the exposed surface or axis. For instance, in wurtzite the dielectric constants for ZnO, ϵ_r, are 8.91 parallel to c-axis ($E \| c$) and 7.77 perpendicular to c-axis ($E \perp c$) [3]. This will affect the electrical and optical properties.

2.1.2 Crystal defects

Crystal defects are inevitable in a real crystal, due to incorporation of impurities during growth. However, in many cases, defects of certain type are delibritely introduced in a crystal to alter the material properties.

There are many kinds of defects, and they are categorized by their dimensions which are point- (0D), line- (1D), plane- (2D) and cluster-defects (3D). In the case of point-defects, a vacancy or a foreign atom can be found in the crystal. Depending on the site of the impurity atom, a *substitutional* or a *interstitial* defect occur (see Fig.2.2). This will, in turn, give rise to different properties.

There are different mechanisms and models related to each type of defect, and the equilibrium concentration of a defect can be described by its formation energy and temperature. Generally, high formation energy and low temperature give low defect concentration. In the case of excess defect concentration, a treatment at elevated temperature, called *annealing*, is used to reduce the defect concentration. This assumes that the high tem-

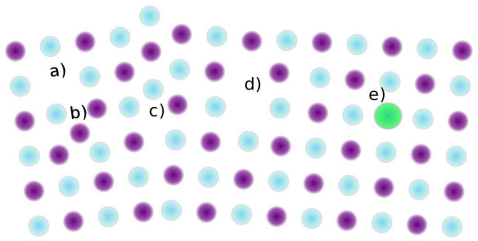

Figure 2.2: Different type of defects. a) vacancy, b) interstitial, c) dislocation, d) divacancy and e) substitutional.

perature does not change the crystal structure.

When two materials of different lattice parameters are grown on top of each other, the lattice mismatch creates strain at the interface which can cause large amount of defect concentration. For that reason, a direct transition between two material may perform poorly. However, the strain can be relaxed by growing a buffer layer of different material which has an intermediate lattice constant.

2.2 General solid state and semiconductor physics

2.2.1 Energy bands

Described by quantum physics, electrons in an atom are forced to occupy discrete levels of energies obtaining different *states*, due to the interactions between the protons and other electrons. However, when electrons are confined in a periodic potential, e.g. in a crystal lattice, these discrete energy levels become *energy bands* separated by *band gaps*. Different material characteristics can be extracted by examining where the electrons are occupied with respect to the energy bands, which in turn determines whether a material is a metal, a semiconductor or an insulator. At 0 K, electrons will occupy the lowest states, and if an energy band is partially filled with electrons, a metal is obtained (see Fig.2.3). On the other hand, if the up-

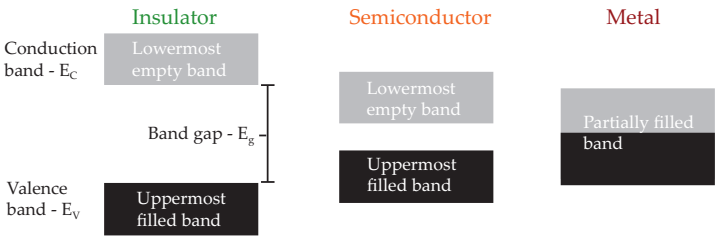

Figure 2.3: Electron occupation at 0 K and the definition of insulator, semiconductor and metal.

permost filled band is completely filled, a semiconductor or an insulator is achieved. The difference between a semiconductor and an insulator is then determined by the energy distance between this filled band, called *valence band*, and the lowermost empty band, called *conduction band*.

As the temperature is raised, electrons are thermally excited pass the band gap to the conduction band. An empty state is then left behind in the valence band, called *hole*. A hole is referred to as a quasi-particle which have both a positive charge and a mass. Since electrons are fermions, their concentration in the conduction band are determined by the Fermi-Dirac distribution and can be approximated (when $E_C - E_F > 3kT$)[1] as shown in Eq. 2.1.

$$n = \int_{E_C}^{\infty} f(E)N(E)dE \approx N_C \cdot exp\left(-\frac{E_C - E_F}{kT}\right) \tag{2.1}$$

where

$$N_C = 2\left(\frac{2\pi m_n^\star kT}{h^2}\right)^{3/2}, \tag{2.2}$$

$m_n^\star$ is the effective mass of an electron, N(E) is the density of states, N_C is the effective density of states in conduction band and E_F is the Fermi-level. A similar expression can be found for the hole concentration in the valence band (2.3).

$$p = \int_0^{E_V} (1 - f(E))N(E)dE \approx N_V \cdot exp\left(-\frac{E_F - E_V}{kT}\right) \tag{2.3}$$

[1]Under this condition, the approximation contains an error of less than 0.24%.

where

$$N_V = 2\left(\frac{2\pi m_p^\star kT}{h^2}\right)^{3/2}. \tag{2.4}$$

A schematical drawing of a band structure is shown in figure 2.4. This diagram is in a coordinate system of energy with respect to k-vector. The meaning of k-vector is related to the momentum of lattice atoms, which can be derived through the investigation of a periodic crystal structure in its reciprocal space. Details can be found in, for instance, Ref. [4]. A band gap can be referred to as a *direct band gap*, when the lowest part of the conduction band is directly above the highest part of the valence band. In this case, a photon[2] with energy large than the band gap is sufficient to excite an electron from the valence band edge (VBE) to the conduction band edge (CBE). Excitation of an electron in an *indirect band gap* requires a change in momentum, provided by the lattice atoms, in addition to the photon. Due to the additional requirement, any interactions between the conduction band (CB) and the valence band (VB) become less probable than a direct band gap.

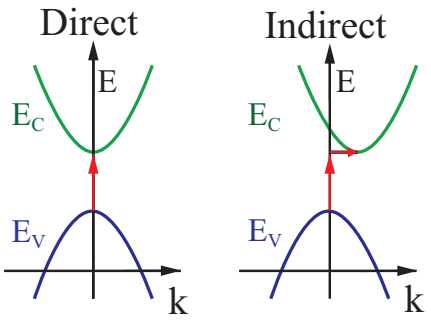

Figure 2.4: Schematical drawing of a direct and an indirect band gap.

[2]A photon is the particle interpretation of light. Its energy is given by the frequency or the wavelength, $E = hf$, where h is the Plancks constant and f is the frequency.

2.2.2 Electrical conductivity and doping

The electrical conductivity, σ, of a semiconductor is determined by the number of electrons and holes in CB and VB, respectively, which is indicated by the Fermi-level in Eqs.2.1 and 2.3, and it is expressed as

$$\sigma = q(n\mu_n + p\mu_p), \tag{2.5}$$

where q is the elementary charge, $\mu_{n(p)}$ is the mobility of electron (hole), n and p are the concentration of electron and hole, respectively.

In an ideal semiconductor at room temperature (RT), only thermally excited electrons exist in CB (and holes in VB). However, the charge carrier concentration (electron or hole) can be modified by introducing foreign atoms. The process of inserting foreign atoms into a material is called *doping*, and it turns an undoped (*intrinsic*) semiconductor into a doped (*extrinsic*) one. By adding an atom which donates an electron, called *donor*, the electron concentration will increase and the Fermi-level is lifted closer to CB. The opposite happens with an atom which accepts an electron, called *acceptor*. If a material is doped such that the Fermi-level is above its intrinsic level, the material is called n-type material. The opposite is called a p-type material.

For large doping concentrations, the Coulomb interaction between electrons, holes and ionized atoms needs to be considered. The resulting behavior is a reduction in the band gap, called *band gap narrowing*. Many empirical models can be found for this effect. As an example, the Slotboom model predicts a band gap narrowing in silicon (Si) by

$$\Delta E_g = dE_{g0} + E_{bgn}\left(ln\left(\frac{N}{10^{17}}\right) + \sqrt{\left[ln\left(\frac{N}{10^{17}}\right)\right]^2 + 0.5}\right), \tag{2.6}$$

where $dE_{g0} = -4.795 \times 10^{-3}$, $E_{bgn} = 9 \times 10^{-3}$ and N is the doping concentration.

2.2.3 pn-junction

2.2.3.1 Principle

A pn-junction can be achieved by combining a p-type and an n-type semiconductor. If both the semiconductor materials are the same, it is called a *homojunction*, otherwise it is a *heterojunction*. Upon combining, the difference in the chemical potential[3] forces the electron from the n-type material over the junction, until the potential is aligned (while keeping a continuous vacuum level), resulting in an electrostatic potential barrier, V_0 between the two materials (see Fig.2.5). A zone with approximately no free charge carriers appears at the interface, called depletion zone (W) or space charge region (SCR).

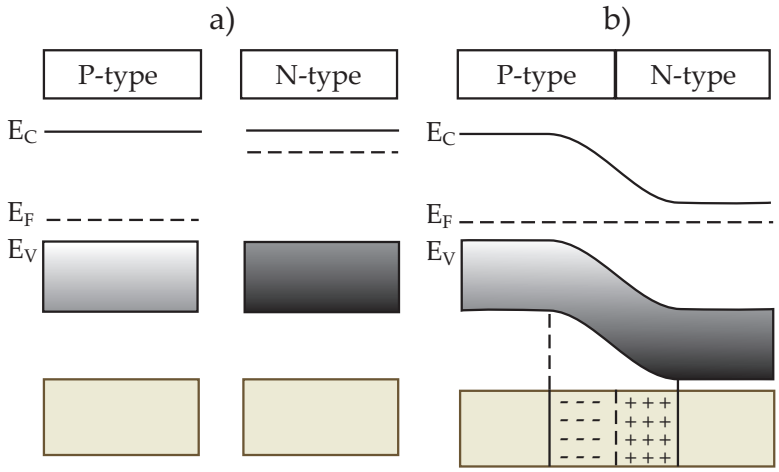

Figure 2.5: Showing the concept of band alignment, where a) a p-type and an n-type material are separated at the beginning. b) The Fermi-levels of both materials align and the energy bands, E_C and E_V, bend as a result of carrier transfer and forming a depletion zone.

Majority carriers[4] are being repelled outside this zone by the electrical

[3]The difference between the chemical potential and the Fermi-level is given by $\mu = E_c - \frac{1}{2}E_F + \frac{3}{4}kT\ ln\left(\frac{m_p^*}{m_n^*}\right)$. A more philosophical interpretation of the subject can be found in the work by M. R. A. Shegelski [5].

[4]Majority carriers are the type of charge carrier corresponding to the type of doping

field. However, some thermally excited majority carriers with sufficient energy, which is the tail of the Fermi-distribution, are able to surmount the potential barrier[5] and reach to the other side of the zone. At equilibrium, this process is balanced out by minority carriers being swept by the electric field in the depletion region (*drift current*). However, the latter process is independent of the external voltage, whereas the thermal excitation of majority carrier over the potential barrier is exponentially dependent on the external voltage. Under forward bias, the potential barrier is lowered, allowing a large current, see Fig.2.6*b*. While the opposite happens in the revers bias, see Fig.2.6*c*.

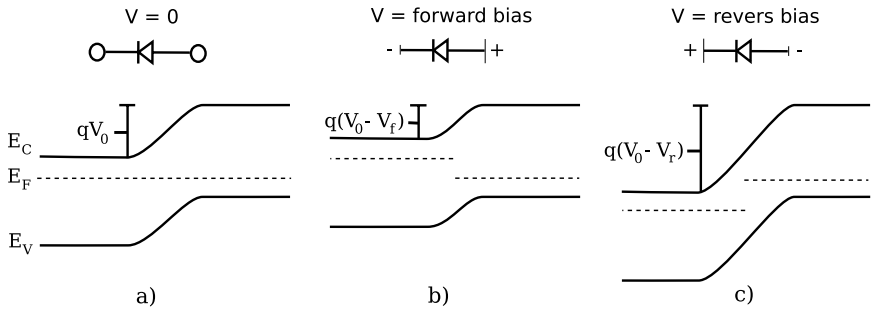

Figure 2.6: The depletion width, band diagram and Fermi-level change according to the applied voltage, resulting in a change in the total current.

The following derivations of important equations related to a pn-junction can be found in, e.g. Ref. [6].

2.2.3.2 The depletion width

To calculate the depletion width as a function of applied voltage analytically, an approximation called *depletion approximation* needs to be made. It states:

- The depletion width, W, is abrupt and consists of no free charge carriers, i.e. $p = n = 0$.

in a material, e.g. electrons are the majority carriers in a n-type material. The opposite, minority carrier, corresponds to holes in this case.

[5]This electrostatic potential at zero bias is referred to as the *built-in potential*.

- The material outside W is neutral.

The one dimensional Poissons equation is considered for the electric field in the depletion zone,

$$\frac{dE}{dx} = \frac{q}{\epsilon_r \epsilon_0}(p - n + N_d^+ - N_a^-), \tag{2.7}$$

where N_d^+ and N_a^- are the concentration of ionized dopants, ϵ_r is the relative permittivity and ϵ_0 is the permittivity of free space. With the approx-

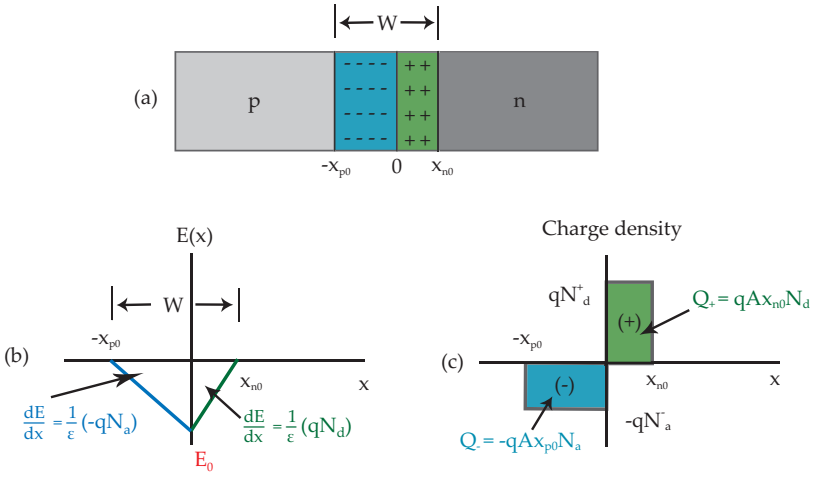

Figure 2.7: Space charge and electrical field distribution in the depletion zone which can be affected by external voltage and doping concentration. Figure inspired by Ref. [6].

imation of p=n=0 in W, the assumption of complete ionization of dopants in W and the definition of a pn-junction shown in Figure 2.7(a), the equation can be rewritten to

$$\frac{dE}{dx} = \begin{cases} \frac{q}{\epsilon_r \epsilon_0} \cdot (-N_a) & -x_{p0} < x < 0 \\ \frac{q}{\epsilon_r \epsilon_0} \cdot N_d & 0 < x < x_{n0} \end{cases} \tag{2.8}$$

This equation is illustrated in Figure 2.7(b) and shows the largest absolute E-field as E_0. Solving Eq.(2.8) for E, one obtains:

$$E_0 = -\frac{q}{\epsilon_r \epsilon_0} N_d x_{n0} = -\frac{q}{\epsilon_r \epsilon_0} N_a x_{p0}. \tag{2.9}$$

Since the definition between electric field and electric potential is

$$E(x) = -\frac{dV}{dx}. \tag{2.10}$$

The contact potential (also referred to as the built-in potential), V_0, and the applied voltage which is defined positive in forward bias, V_a, becomes

$$V_0 - V_a = -\int_{-x_{p0}}^{x_{n0}} E(x)dx = -\frac{1}{2}E_0(x_{n0} + x_{p0}) = \frac{1}{2}\frac{q}{\epsilon_r\epsilon_0}N_d x_{n0}W. \tag{2.11}$$

Noticing that $x_{x0} = WN_a/(N_a + N_d)$, the depletion width becomes

$$\boxed{W = \left[\frac{2\epsilon_r\epsilon_0(V_0 - V_a)}{q}\left(\frac{N_a + N_d}{N_a N_d}\right)\right]^{1/2}} \tag{2.12}$$

2.2.3.3 Capacitance of pn-junction

The general formulation of capacitance is

$$C = \left|\frac{dQ}{dV'}\right| = \left|\frac{dQ}{d(V_0 - V)}\right| \tag{2.13}$$

In the depletion approximation, Q is found to be (Fig.2.7*c*)

$$|Q| = qA\frac{N_d N_a}{N_d + N_a}W = A\left[2q\epsilon_r\epsilon_0(V_0 - V)\frac{N_d N_a}{N_d + N_a}\right]^{1/2} \tag{2.14}$$

Combining Eq.(2.13) and 2.14 one obtains

$$C = A\sqrt{\frac{q\epsilon_r\epsilon_0}{2(V_0 - V)}\left(\frac{N_d N_a}{N_d + N_a}\right)} = \frac{\epsilon_r\epsilon_0 A}{W} \tag{2.15}$$

This approximated capacitance resembles a setup of two capacitor plates with a distance of W from each other, which in many cases is sufficient to describe phenomena. Anyhow, a more accurate description of the capacitance will be given in Section 2.2.4.2, which is often applied for a Schottky contact.

2.2.3.4 The diode equation

The potential dependent charge flow through a diode is governed by 1) thermal excitation of charge carriers over the potential barrier (*thermionic emission*) and 2) movement of injected carriers away from the depletion region to the contacts. These two processes exist in series, which means that the slowest one limits the charge flow. In a pn-junction, where both materials are semiconductors, process 2) is controlled by the diffusion of injected carriers (with an effective diffusion velocity $v_d = D_n/n(dn/dx)$, where D_n is the diffusion constant of electron), and it is considered to be the slowest[6]. Thus, in the *diffusion theory* which describes the current-voltage dependence in a pn-junction, the diode is limited by the diffusion current. Based on these principles, the *diode equation* can be derived as

$$J = q\left(\frac{D_p}{L_p}p_n + \frac{D_n}{L_n}n_p\right)\left[exp\left(\frac{qV}{kT}\right) - 1\right] = J_0\left[exp\left(\frac{qV}{kT}\right) - 1\right], \quad (2.16)$$

where $L_{n(p)}$ is the diffusion length of electron (hole) which is the average distance before a charge carrier recombines. It shows an exponential increase in forward bias, while the revers/leakage current density is controlled by the constant J_0. The details of this derivation are given in Appendix A.2.

2.2.4 Schottky contact

2.2.4.1 Principle

A Schottky contact is similar to a pn-junction, where one side of the junction is replaced by a metal. The band alignment follows the same rule as for a pn-junction (see Fig.2.8). However, different properties arise depending on the work-function (Φ_M) of the metal, the type of doping and the electron affinity (χ_S) of the semiconductor, and this setup can result in an Ohmic or a Schottky contact. By definition, an Ohmic contact has a linear relation between current and applied voltage. Whereas in a Schottky contact, the current dependence resembles the diode equation in forward bias and then strongly depends on the barrier height in reverse bias.

[6]This is not the case in a short diode, when the gradient is increased [7].

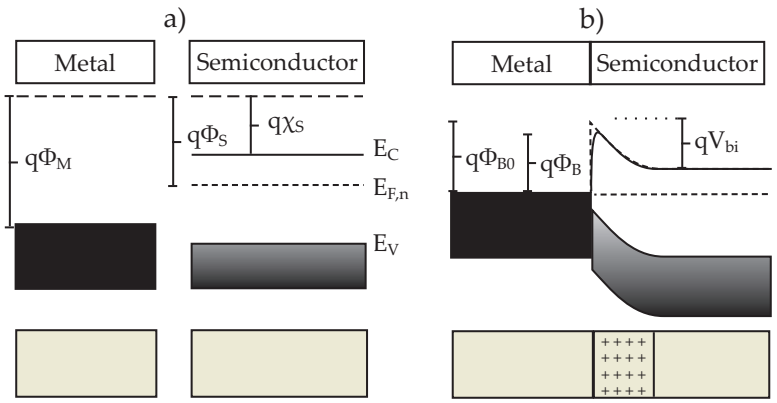

Figure 2.8: Band alignment between a metal and an n-type semiconductor. a) Metal and semiconductor before combining. b) Band alignment and barrier heights.

The barrier height, being an important quantity, can be affected by, for instance, the *image force*. When an electron approaches a metal interface, positive charges are induced in the metal as if there exists a positively charged particle on the other side. Electrons seeing this particle/image will experience an attraction force. The barrier height can, for instance, be lowered to $q\Phi_B$, see Fig.2.8.

In contrast to a pn-junction, a Schottky contact is a *majority carrier device*.

2.2.4.2 The capacitance

The previously described capacitance equation, Eq.2.15, can be improved by not making the approximation of an abrupt depletion edge. The resulting Poissons equation becomes

$$\frac{d^2V}{dx^2} = \frac{q}{\epsilon_r\epsilon_0}N_d(1-e^Y) \tag{2.17}$$

where

$$Y = -\frac{q}{kT}[V(x) - V(\infty)] \tag{2.18}$$

Under this modification, the capacitance becomes

$$C = A\sqrt{\frac{q\epsilon_r\epsilon_0 N_d}{2(V_{bi} - V - kT/q)}} \tag{2.19}$$

The details of this expression can be found in Ref. [8].

2.2.4.3 The thermionic emission theory

Recalling the limitation of charge flow in a pn-junction, where the current is limited by the diffusion current in the semiconductor, the current in a Schottky contact is limited by the thermionic emission from the semiconductor to the metal, and that the emitted charge carriers are quickly swept away from the junction. Thus, the gradient of the quasi-Fermi level[7] in the metal is small/negligible. At equilibrium, thermionic emission current density from semiconductor to metal, J_{sm}, is balanced out by the opposite, J_{ms}.

The thermionic emission current density from semiconductor to metal, evaluated with the elementary kinetic theory, is

$$J_{sm} = \frac{qN_c\overline{v}}{4}\, exp\left[\frac{-q(\Phi_b - V)}{kT}\right] \tag{2.20}$$

Whereas the current density from metal to semiconductor is unaffected by the external voltage (disregarding the image force) and is solely determined by the barrier height:

$$J_{ms} = \frac{qN_c\overline{v}}{4}\, exp\left(\frac{-q\Phi_b}{kT}\right), \tag{2.21}$$

where $\overline{v} = (8kT/\pi m^*)^{1/2}$ is the average of the Maxwellian distribution of velocities. Inserting for N_c from Eq.2.2, the total current density becomes

$$J = J_{sm} - J_{ms} = J_0\left[exp\left(\frac{qV}{kT}\right) - 1\right] \tag{2.22}$$

[7]Similar to Fermi-level, the quasi-Fermi level of electron or hole describes the charge carrier concentration. Quasi-Fermi levels are used when excess carriers are present, such as injected or light excited carriers.

with

$$J_0 = A^* T^2 exp\left(\frac{-\Phi_b}{kT}\right), \qquad A^* = \frac{4\pi q m^* k^2}{h^3}, \tag{2.23}$$

where A^* is the effective Richardson's constant and m^* is the effective mass of the majority carrier in the semiconductor.

In the non-ideal case, when other effects such as image force, thermal generation and series resistance, Eq.2.22 is modified to

$$\boxed{J = J_0\, exp\left(\frac{q(V - IR_s)}{\eta kT}\right)\left[1 - exp\left(\frac{-q(V - IR_s)}{kT}\right)\right]}, \tag{2.24}$$

where η is the ideality factor and R_s is the series resistance. The ideal case is when $\eta = 1$.

Other charge transfer mechanisms occur when the doping concentration in the semiconductor becomes high. They are related to tunneling and are called *thermionic field emission* ($10^{17} cm^{-3} \leq N_D \leq 10^{19} cm^{-3}$) and *field emission* ($10^{19} cm^{-3} \leq N_D$) (See Fig.2.9). Details about thermionic field emission and field emission can be found in Ref. [9] (p. 106).

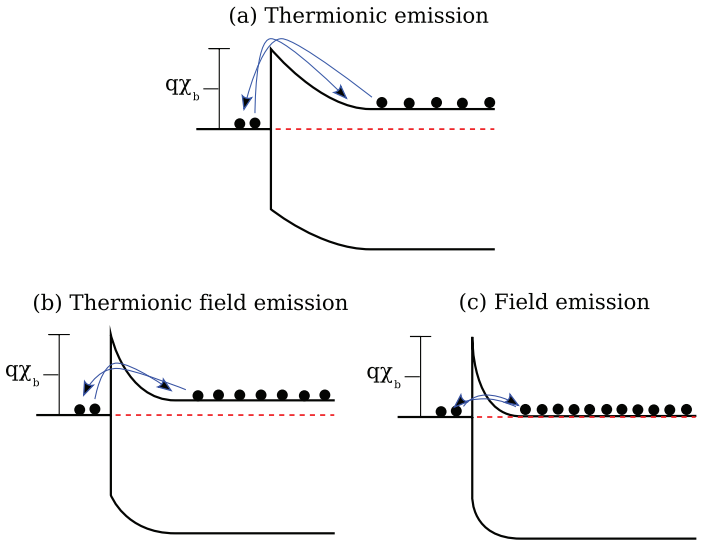

Figure 2.9: Illustration of electron flow during a) thermionic emission, b) thermionic field emission and c) field emission.

2.2.5 Heterostructure

As mentioned in the Section 2.2.3, a heterostructure consists of a junction between different semiconductor materials. The major changes arise from the difference in electron affinity and band gap, which in turn enables the tailoring of the properties of such a junction. For instance, electrons will not experience the same potential barrier as for holes, which is important in a bipolar transistor. On the other hand, structural changes in terms of lattice mismatch, contribute significantly to interface defects. As an example, *Fermi-level pinning* occurs when the interface defect concentration becomes too high and screens the communication between both sides. This might cause a band alignment only on one side and it bends according to the defect level.

Heterostructures are categorized into three groups based on the differences between the energy band of the semiconductors. They are referred to as *Type I* to *Type III* by the name *straddling gap*, *staggered gap* and *broken gap* (see Fig.2.10). Being the characteristics of heterostructure, the band off-

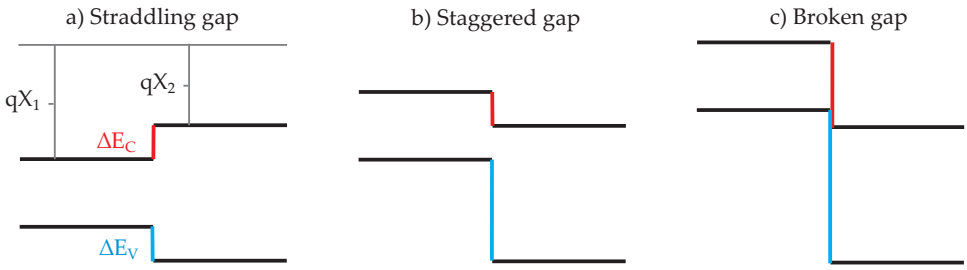

Figure 2.10: Categories of heterostructure, which is based on the band gap mismatch.

sets (ΔE_C and ΔE_V) are of great interests. Based on Fig.2.10, these energies are solely determined by electron affinities and band gaps of the materials involved. However, this is not always true, and many theories/rules are deduced to predict the band offsets. The *Andersons model*, also referred to as the *electron affinity model*, disregards any lattice mismatch between the semiconductors and states that the band offsets are directly related to the

electron affinities and the band gaps, such that

$$\Delta E_C = \chi_1 - \chi_2 \tag{2.25}$$

and

$$\Delta E_V = (E_{g,1} + \chi_1) - (E_{g,2} + \chi_2) \tag{2.26}$$

where subscript 1 and 2 represent different semiconductor material. This model has proven to work well in heterostructures such as Si/Ge, InAs/GaSn and CdSe/InP. However, in some compound semiconductors, such as GaAs/AlAs, this theory fails and replaces by the *anion rule*. It is believed that the valence band structure relies mostly on the anions in a material. Thus, materials with common anion is predicted, by this rule, to have a less discontinuity in the valence band, but without any quantitatively estimations. However, the structure GaAs/AlAs is predicted to have a ratio $\Delta E_V/\Delta E_C = 0.73$ by Andersons model, while the experimental ratio is 0.6.

To illustrate one of the differences between homo- and heterojunction. Let us consider the electric field based on the depletion approximation. Once again, the electric field is obtained through the Poissons equation. Requiring charge neutrality, the corresponding electric field for semiconductor 1 and 2 are:

$$E_1(x) = \frac{qN_{D,1}}{\epsilon_{r,1}\epsilon_0}(x_1 + x), \qquad -x_1 < x < 0 \tag{2.27}$$

$$E_2(x) = \frac{qN_{D,2}}{\epsilon_{r,2}\epsilon_0}(x - x_2), \qquad 0 < x < x_2 \tag{2.28}$$

Note the discontinuity in the electric field due to the relative dielectric constant of semiconductors.

2.2.6 Defects and traps

Having the knowledge about pn-junction (homo- and heterostructure), Schottky contact and the depletion region, it is important to recall the discussion about defects and dopants as they determine the performance of a device. Much of the content in this section follows that of Ref. [9].

Defects and dopants can generate energy states *within* the band gap, called *defect level*. If a defect level is situated near a band edge (E_c or E_v), it is referred to as a *shallow level*. Whereas a defect level further away, is referred to as a *deep level*. There is no distinct difference between these two terms. However, shallow and deep levels are also often referred to as dopants and generation-recombination centers (G-R), respectively.

2.2.6.1 Emission and capture mechanisms

As there are energy states within the band gap, excitation (as well as de-excitation) of charge carriers with less energy than E_g is now possible, and four charge carrier exchange mechanisms exist between a defect level and the energy bands, see Fig.2.11. A recombination or generation process is simply an event that involves *both* energy bands, i.e. Fig.2.11 *a* is followed by *c*, or *b* is followed *d*, respectively.

Whereas a *trapping* process can be thought of as an event that involves only *one* band, i.e. Fig.2.11 *a* is followed by *b*, or *c* is followed by *d*.

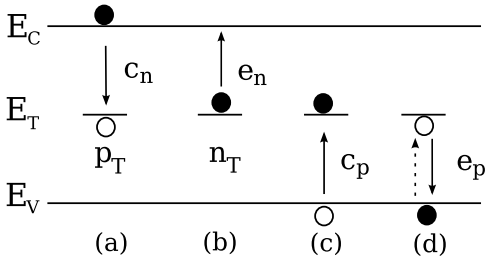

Figure 2.11: Definition of capture and emission of electron and hole. a) Electron capture, b) electron emission, c) hole capture and d) hole emission.

2.2.6.2 Time dependence of trap occupancy

As the exchange of charge carriers between energy bands and the defect levels (thereby changing the electron and hole concentration in E_c and E_v)

happens over a time, t, it is important to take into account the time dependence of these mechanisms. Considering one deep level with concentration $N_T = n_T + p_T$, which is either occupied by electron, n_T, or hole, p_T. The change in the electron concentration in E_c becomes (Fig.2.11*b* - *a*)

$$\frac{dn}{dt} = e_n n_T - c_n n p_T \tag{2.29}$$

and for the hole concentration in E_v (Fig.2.11*d* - *c*)

$$\frac{dp}{dt} = e_p p_T - c_p p n_T, \tag{2.30}$$

where n and p are the carrier concentration in E_c and E_v respectively, $e_{n(p)}$ is the emission rate of electrons (hole) and $c_n n$ ($c_p p$) is the capture rate of electrons (holes). The capture term[8] ($c_n n$ or $c_p p$) is slightly different than the emission term because it requires charge carriers in the respective energy bands in order to capture carriers, and it can be expressed as

$$c_n n = v_{th} \sigma_n n \tag{2.31}$$

, where $v_{th} = \sqrt{3kT/m_n^*}$ is the electron thermal velocity and σ_n is the electron capture cross section. The electron occupancy of the defect level at any given time can be expressed as

$$\frac{dn_T}{dt} = \frac{dp}{dt} - \frac{dn}{dt} = (c_n n + e_p)(N_T - n_T) - (c_p p + e_n) n_T \tag{2.32}$$

With the assumption of constant p and n outside the depletion region, the solution of the above equation becomes

$$n_T(t) = n_T(0) e^{-t/\tau} + \frac{e_p + c_n n}{e_n + c_n n + e_p + c_p p} N_T (1 - e^{-t/\tau}), \tag{2.33}$$

where $n_T(0)$ is the electron occupancy of the G-R defect level at $t = 0$ and $\tau = 1/(e_n + c_n n + e_p + c_p p)$. The steady state occupancy can easily be obtained by the limit $t \to \infty$.

[8] the definition of the electron capture rate , $c_n n$ ($= v_{th} \sigma_n n$), might be different from other literatures (sometimes $c_n = v_{th} \sigma_n n$), but written in this form clarifies the requirement of available charge carriers in the energy bands in order to capture carriers.

As an example, consider an n-type substrate ($n \gg p$) in a situation where a p^+n-junction is reverse biased (at $t > 0$) from zero bias (at $t \leq 0$). Assuming that the electron emission dominates at $t > 0$ ($e_n \gg e_p$) and since there are no electrons to capture from E_c in the depletion zone ($n = 0$), Eq.2.33 becomes

$$n_T(t) \approx n_T(0)e^{-t/\tau} = N_T e^{-e_n t} \tag{2.34}$$

2.2.6.3 Emission rate

In equilibrium, where $\frac{dn}{dt} = 0$ and $\frac{dp}{dt} = 0$, and applying the *principle of detailed balance* which states that "under equilibrium conditions each fundamental process and its inverse must balance independent of any other process that may be occurring inside the material" (Ref. [9] p.307), it can be shown from Eq.2.29 that

$$e_{n0} n_T = c_{n0} n_0 (N_T - n_T), \tag{2.35}$$

where the subscript 0 indicates equilibrium. From Eq.2.1 and knowing that the trap states follow the Fermi-Dirac-distribution

$$\frac{n_{T0}}{N_T} = f(E_T) = \frac{1}{1 + exp[(E_T - E_F)/kT]}, \tag{2.36}$$

Eq.2.35 can be expressed as

$$e_{n0} = c_{n0} n_i exp\left(\frac{E_T - E_i}{kT}\right) \tag{2.37}$$

The *non*-equilibrium of the latter expression can be achieved by removing the subscript 0, which is often performed. However, this practice may lead to errors due to field-enhanced emission and tunneling. Without further considerations,

$$e_n = c_n n_i exp\left(\frac{E_T - E_i}{kT}\right) = v_{th}\sigma N_C exp\left(\frac{E_T - E_C}{kT}\right) \tag{2.38}$$

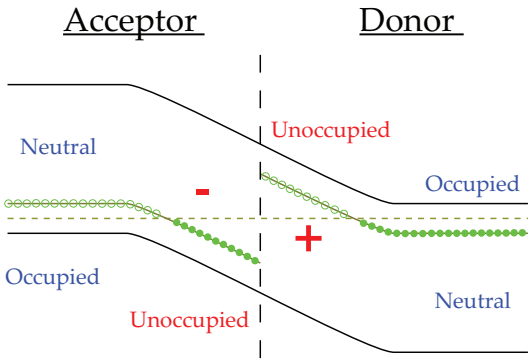

Figure 2.12: Definition of charge state for acceptor and donor with respect to its occupancy.

2.2.6.4 Donor and acceptor

Whether a defect is donor or acceptor, is solely determined by its charge state when it is occupied or unoccupied by an electron or a hole. The definition is schematically shown in Fig.2.12. However, the doping type of a defect can be extracted by analyzing their valence electrons compared to the host atom. As an example, phosphorus (which has five valence electrons) can substitute for silicon (which has four valence electrons) in a silicon crystal and become positively charged by donating its extra electron (becoming unoccupied).

2.2.7 Photocurrent

Photocurrent is the generation of electrical current by exposure of light/photons. When a semiconductor is exposed to photons with energy larger than its band gap energy, electrons can be excited to the conduction band leaving holes in the valence band. This generation of electron-hole-pairs (EHP) will increase the charge carrier concentration in the semiconductor which decays by recombination. If the EHP are seperated by a driving force before recombining, a photocurrent is achieved. Such driving force can, for instance, be provided by an electric field in the depletion region or a gradi-

ent in the charge carrier concentration.

Taking a pn-homojunction under uniform illumination as an example, an electric field is set up by uncompensated ions in the depletion region. Holes and electrons, from photogenerated EHP within W, will experience this field and drift to the p- and n-side, respectively. Moreover, EHP which are generated *outside* W, but within a diffusion length, can diffuse to the depletion region and be swept to the other side by the electric field. Under these conditions, the photocurrent can be expressed as

$$I_{op} = qAg_{op}(L_n + L_p + W), \tag{2.39}$$

where A is the cross section area of the semiconductor, g_{op} is the optical generation rate per cm^{-3} and L is the diffusion length. Recalling the diode equation, the total current can be expressed as:

$$I_{tot} = qA\left(\frac{D_p}{L_p}p_n + \frac{D_n}{L_n}n_p\right)\left[exp\left(\frac{qV}{kT}\right) - 1\right] - qAg_{op}(L_n + L_p + W) \tag{2.40}$$

This equation is schematically illustrated in Fig.2.13*a*, and an interesting feature is obtained in the fourth quadrant where the current is directed opposite to the applied voltage. Thus, a power can be extracted, and this is utilized in the solar cell. When discussing solar cells, the IV-curve is usually turned up-side-down, i.e. multiplied the current with -1. The extraction power from the fourth quadrant is then given by $P = IV$.

As discussed above, the solar cell is operated in the fourth quadrant, and it is characterized by the *short-circuit current*, I_{sc}, the *open-circuit voltage*, V_{OC}, and the fill factor, f, as illustrated in Fig.2.13*b* The operating conditions which result in the highest power is at V_m and I_m, with

$$P = I_m V_m = f I_{SC} V_{OC} \tag{2.41}$$

In order to achieve high power output, all these parameters should be as large as possible. However, the parameters are highly determined by material properties, defects and doping.

The conversion efficiency is defined as the ratio between input and output power, which can be expressed as:

$$\eta = \frac{P_{out}}{P_{in}} = \frac{f I_{SC} V_{OC}}{P_{in}}, \tag{2.42}$$

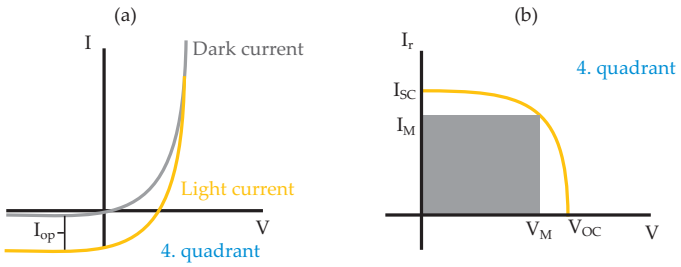

Figure 2.13: IV-characteristic of an illuminated solar cell. The shaded area in b) shows the condition for the highest power output.

where P_{in} is the power of the incident light.

Chapter 3

Zinc oxide

This chapter introduces zinc oxide to highlight the interests and importance of its properties as a transparent conducting oxide and within optoelectronics. Fabrication methods of bulk ZnO will be mentioned in conjunction with issues relating to the bulk wafers.

3.1 Introduction to ZnO

The element Zn, is considered to be the 4th most commonly used metal, the 24th most abundant material (0.007%) in the earth's crust [10] and exists commonly in the nature as ZnS which can be reacted to form ZnO by the roasting process at 1200 $^{\circ}C$ [11],

$$2\,ZnS + 3\,O_2 \rightarrow 2\,ZnO + 2\,SO_2 + 862\,kJ. \tag{3.1}$$

The non-toxic product, ZnO, adapts the wurtzite crystal structure under this condition (and under standard condition for temperature and pressure, i.e. 273 K and 1 atm.) and decomposes into Zn and O_2 above $\sim$2000 $^{\circ}C$ [12]. In electronics, ZnO is a II-VI semiconductor with a direct wide band gap of $\sim$3.36 eV at room temperature which enables it to become transparent to visible light, and thus white in the powder form.

The wurtzite structure of ZnO (space group $P6_3mc$) has lattice parameters of a=3.25 Å and c=5.21 Å , which gives a total of $\sim 8.4\times10^{22}$ atoms per cm^3. In principle, the [0001]-direction is terminated by Zn-atoms (Zn-

face), whereas the $[000\overline{1}]$-direction consists of O-atoms (O-face). A summary of ZnO properties can be found in Table.3.1. Note the large difference in the electron affinity.

Table 3.1: Properties of ZnO.

	Electron	Hole	Ref.
Mobility $[cm^2/Vs]$	100-200	5-50	[13, 14, 15]
Effective mass $[m_*/m_0]$	0.24-0.28	0.59-0.78	[15, 16]
Effective density of states $[cm^{-3}]$	$2.9 - 3.7 \times 10^{18}$	$1.1 - 1.7 \times 10^{19}$	-
Bandgap, $E_g(300K)$ [eV]	3.36 (direct)		[17]
Relative permittivity $(E\|c)$, ϵ	8.50-8.91		[18, 3]
Electron affinity, χ [eV]	3.7-4.45		[19, 20]

Due to its combination of high conductivity and high transparency, ZnO is clasified as a transparent conducting oxide like indium tin oxide (ITO), which already has many applications in the everyday life, such as liquid crystal display (LCD), touch panel and electronic ink. In addition, TCO can have multiple purposes in solar cells or photovoltaics (PV), where it can act as the front-contact, the emitter and as anti-reflection coating (ARC). This can simplify the processing of solar cells significantly in terms of structural complexity. Since zinc is a more abundant element than indium, replacing ITO with ZnO can lead to higher cost efficiency.

ZnO has a superior exciton binding energy of 60 meV compared to that of 24 meV in GaN, which means that EHP are stable at room temperature ($\sim$26 meV) and radiative recombination is more favorable. Hence, ZnO-based light-emitting-diodes (LED) will be very energy efficient. The emitted light is dependent on the band gap of ZnO, but can be engineered with Cd and Mg to a range of 2.65 - 5.0 eV [21, 22], equivalent to a blue to ultraviolet range.

3.2 Fabrication of bulk ZnO

The fabrication step is an important process due to the concentration of impurities and defects which might be introduced. The common ways of fabricating bulk ZnO are through *hydrothermal*, *vapour phase* and *melt growth* techniques. Other structures than wurtzite, i.e. rocksalt can occur at pressure of 8-15 GPa and zinc blende is metastable which requires stabilization with heteroepitaxy using structures such as ZnS and GaAs/ZnS [2].

Hydrothermal

The hydrothermal (HT) process is a growth/synthesis method where solutions are mixed together, sealed in a container and heated in an oven. The growth condition in temperature and pressure for ZnO range around 300-400°C and 70-150 MPa, respectively. Seed crystals are mounted in the chamber separated from the solution with a lower temperature, usually 10-30 °C. Since everything is sealed, reactions happening in the container are diffucult to monitor. By varying, e.g. the pressure, temperature, pH and the ratio between precursors, the crystal growth can be altered.

The growth of bulk ZnO in HT process often uses KOH and LiOH [23, 24], and therefore the product can contain large amount of lithium and potassium, as high as $10^{17}\,\mathrm{cm}^{-3}$ [25]. In addition, due to an anisotropic growth rate where the [0001] direction dominates with a ratio of 3:1, the impurity concentration varies even more spatially, which can affect the device performance significantly. With HT process, the growth rate in the fastest direction is typically $\sim$0.06-0.25 mm/day. The electron mobility with this growth method is typically $\sim$100 cm/Vs [13].

Two providers for hydrothermally grown ZnO wafers are Tokyo Denpa (from Japan) and SPC Goodwill (from Russia). One of their differences in deep level defects was highlighted by S. Seto et al [26], using photoluminescence (PL). Compared to other methods used for ZnO, HT growth has the advantage with its scalability which is suitable for high volume industrial purposes.

Vapour phase

A method for growing ZnO that results in less impurities and avoids the use of solutions is vapour phase. This method utilizes a horizontal lying tube where powder ZnO and seed crystals are placed at separate ends with a temperature around 1150°C and 1100°C, respectively. Together with a carrier gas, H_2, reaction (3.2) is assumed to happen at the high temperature end and the revers reaction at the opposite end.

$$ZnO(s) + H_2(g) \rightarrow Zn(g) + H_2O(g) \tag{3.2}$$

For a growth of 150-175h, a 2in diameter crystal with thickness of 1 cm can be made. In this condition, charge carrier concentration and mobility are $6 \times 10^{16}\,\mathrm{cm}^{-3}$ and 205 cm/Vs, respectively, according to Hall-measurement [27].

Melt

At the present, the growth technique with the least amount of impurities is from high pressurized melt growth, by e.g. Cermet Inc. [28]. A cooled boule with ZnO is selectively heated by radio frequency in an oxygen atmosphere of 5 MPa. This avoids contamination from the crucible and the dissociation of ZnO into ZnO_{1-x}. With this method, a growth rate of 1-5 mm per hour is achieved. Typical values for electrical parameter of melt grown ZnO from Cermet can be found in Table 3.2.

Table 3.2: Typical electrical properties of melt grown ZnO from Cermet Inc. Table adapted from J. Nause et al [28].

Temperature $[K]$	Resistivity $[\Omega cm]$	Carrier concentration $[cm^{-3}]$	Mobility $[cm^2V^{-1}s^{-1}]$
296	9.430×10^{-2}	5.045×10^{17}	131
78	5.770×10^{-1}	3.640×10^{16}	298

3.3 Intrinsic defects

Unintentionally, all as-grown bulk ZnO are n-type with the carrier concentration $\sim 10^{16} - 10^{18}\,\mathrm{cm}^{-3}$. However, the origin to this behavior is still controversial. Zinc interstitial, Zn_i, and oxygen vacancy, V_O, have been the candidates for this seemingly intrinsic carrier concentration, and the nature of these defects have been studied theorectically via density functional theory (DFT). According to Janotti and Van de Walle [29], using local denisty approximation (LDA) and LDA+U, none of the intrinsic defects (V_O, Zn_i and Zn_O) can cause the n-type conductivity due to their high formation energy under n-type conditions, even though Zn_i and Zn_O are calculated to be shallow defects. Zn_O has even high formation energy in zinc-rich condition, which makes it very unlikely to contribute in significant concentrations.

The exact electrical level positions of these defects cannot be determined by DFT, due to the well-known underestimation of band gap by using LDA. However, experimental studies have revealed a defect level (E3) at 0.3 eV below the CBE, irrespective to fabrication method of bulk ZnO. Therefore, E3 has often been proposed as a candidate for the intrisic defect of either Zn_i or V_O [30, 31, 32]. T. Frank *et al.* [33] performed a radiation study on vapour phase ZnO, based on the different displacement energy of Zn and O of 41.1 eV and 18.5 eV, respectively. Supported by an annealing study, they suggested that the defect level at 0.3 eV and 0.6 eV below CBE were caused by Zn_i and V_O, respectively.

In Ref. [29], A. Janotti and C. G. Van de Walle also reported that the intrinsic acceptors O_i and O_{Zn} have high formation energies, suppressing them to act in significant concentrations. However, the intrinsic acceptor V_{Zn} has low formation energy in n-type samples and is likely a compensating defect.

3.4 Extrinsic defects

Donor

Reproducible n-type doping can easily be achieved by various group-III elements. High n-type conductive thin films with doping of B, Al, Ga or In have been produced by many groups with resistivities as low as $10^{-4}\,\Omega$cm [34,35,36]. With Al or Ga, the transparency of the films reached above 91% and 85% in wavelength of 400-1200 nm, respectively, which is highly suitable for applications as TCO. As group-III elements are donors in substitution of Zn, n-type doping can also be achieved with group-VII elements in oxygen-site, such as Cl and I.

The role of hydrogen has been investigated in the connection with the unintentional n-type doping. Unlike that in other semiconductors, hydrogen exists solely as a positive ion, acting as a shallow donor [37,38].

Acceptor

Like many other wide band gap semiconductors, such as ZnSe and ZnTe, achieving both n-type and p-type doping is difficult for ZnO [15]. P-type doping in ZnO is met by various issues: 1) low solid solubility, 2) being compensated by native defects, 3) being amphoteric, which means that an added element acts as both donor and acceptor and 4) deep levels.

Although many research groups have reported p-type thin films ZnO, the reproducibility and stability are still unsatisfactory. The known elements which provide the p-type doping are As, N, Sb, Li and F. The As-atoms have shown to substitute for Zn, which acts as n-doping [39]. However, As_{Zn} induces 2 V_{Zn} which effectively gives a shallow acceptor [40].

The solid solubility of Li in ZnO is high, which enables high doping concentration . However, the acceptor Li_{Zn} has its counterpart the donor Li_i which can lead to semi-insulating ZnO.

3.5 Previous work

In this section, some of the previous work relevant to this thesis will be presented.

3.5.1 Schottky contacts to ZnO

The earliest report on Schottky barrier contacts to ZnO can be found in 1965 by C. A. Mead [41]. The measured Schottky barrier height (SBH) with Au and Ag were 0.71 and 0.68 eV, respectively, with an ideality factor of 1.05. However, in the later studies, reviewed by Özgür *et al.* [2] (p.82), large variations in the barrier height is observed for Au ranging from 0.50 eV to 0.71 eV. Similar behavior is experienced with other metals, such as Pt, Pd and Ag, and the ideality factor varied between 1.15 and 4.78. In addition, time-degradation and reproducibility of the contacts have proven to be a great challenge.

The quality issue of ZnO Schottky contact in term of high ideality factor and low rectification in the IV-curves has been addressed by many publications. One proposal by Polyakov *et al.* [42] regarding these issues is to simply preclean the samples with an organic solvent instead of HCl or HNO_3. More extensive studies have been made on the surface properties, such as surface pretreatment with oxygen plasma [43], hydrogen peroxide [44] and ozone [45]. Moreover, the polarity difference between the O-face and the Zn-face of ZnO has proven to give a significant different rectification in the IV-characteristics, which is highlighted by M. W. Allen *et al.* [46] (See Fig.3.1) and T. Maqsood [25].

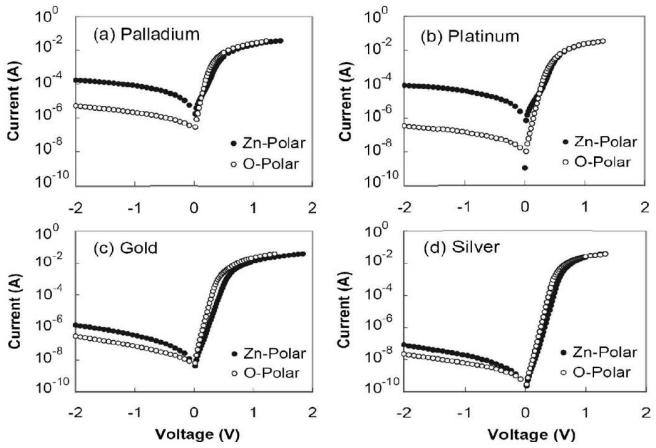

Figure 3.1: Typical IV-characteristics at room temperature for various metal Schottky contact on Zn- and O-face measured by M. W. Allen *et al.* [46].

In the work by M. W. Allen *et al.*, Pd, Pt, Au and Ag Schottky barrier diode (SBD) on Zn- and O-face have been investigated for its IV-characteristics. A trend of lower leakage current for O-face SBD than Zn-face can be observed. Althought silver has the lowest work function, it has been reported with the highest rectification. It is suggested that an oxidation of silver happens at the interface, giving rise to a layer of silver oxide which has a work function, theoretically estimated, up to 7.0 eV. As for the low rectification of Pd Schottky, Y. Dong *et al.* [47] suggested in a later study that an indiffusion of hydrogen to the Pd/ZnO-interface, due to the high solid solubility of hydrogen in Pd, can increase the tunneling effect.

Extensive studies on the surface morphology and electrical properties after hydrogen peroxide treatment at different temperature and duration are performed by C. C. Ling *et al.* [48] and Q. L. Gu *et al.* [32]. Large detoriation can be seen after 30min in boiling hydrogen peroxide (See Fig.3.2). However, no direct relation is observed in the IV-characteristics from that threatment (See Fig.3.3).

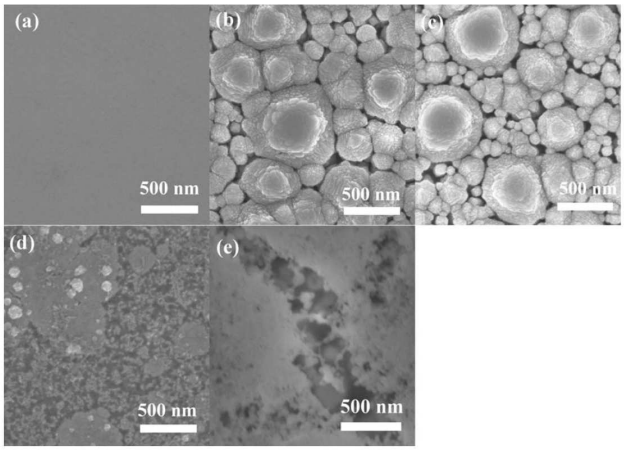

Figure 3.2: SEM image of ZnO surface morphology of a) untreated sample, b) 100°C for 3min, c) 100°C for 30min, d)boiling for 3min, e)boiling for 3min in hydrogen peroxide, measured Q. L. Gu et al. [32].

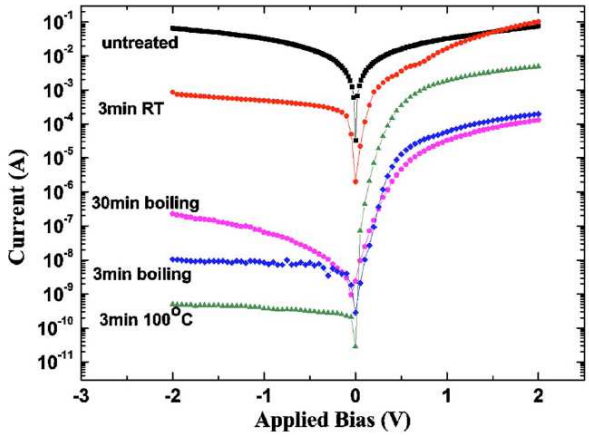

Figure 3.3: IV-characteristics of Au/ZnO-SBD with different pretreatment in hydrogen peroxide, measured by Q. L. Gu et al. [32].

A study of Pd Schottky contact quality with 5 minutes of pre-deposition threatment in hydrogen peroxide (Fig.3.4) has been performed by R. Schifano *et al.* [44], where the rectification reaches up to 8 orders of magnitude. Moreover, the contact quality in terms of rectification differs only slightly after 80 days. The reported ideality factor in revers bias is close to unity which is the lowest reported value till now. However, this value changes rapidly in voltage above +0.5 V, and this is suggested as due to tunneling, interfacial layer and surface recombination.

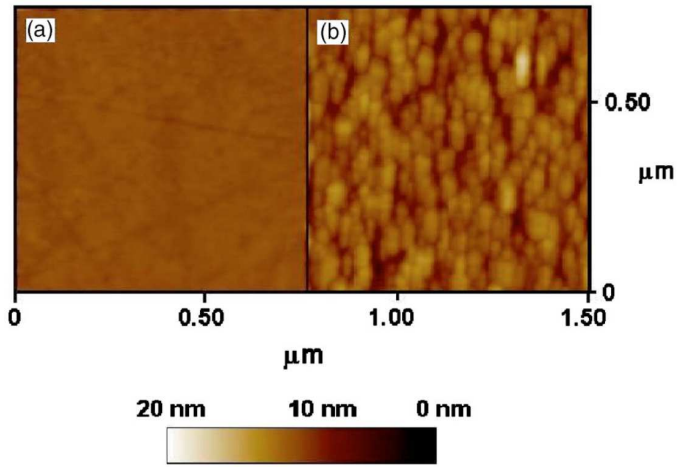

Figure 3.4: AFM amplitude image of ZnO O-face prio to (a) and after 5 minutes threatment in hydrogen peroxide. Figure adapted from Ref. [44].

Table.3.3 summarizes some recently reported data on Schottky contacts. From the table, a large variation between SBH and ideality factor can still be seen.

Table 3.3: Summary of some of the recently (year 2006-2009) reported Schottky contacts on Zn- or O-face n-ZnO with the SBH determined by IV or CV (IV | CV) and sorted chronologically.

Contact material	Type of ZnO	Deposition method	$\Phi_B[eV]$ IV | CV	Ideality factor n	Ref.
Au	Melt (C)	E-beam evaporator	Zn: 0.71 | 0.70 O: 0.69 | 0.70	1.4 1.1	[46]
Ag			Zn: 0.78 | 0.80 O: 0.77 | 0.80	1.2 1.1	
Pd			Zn: 0.55 | - O: 0.59 | 0.59	2.0 1.2	
Pt			Zn: 0.55 | - O: 0.68 | 0.72	2.0 1.1	
Silver oxide	HT (TD)	Reactive rf sputtering	Zn: 1.20 | 1.20 O: 0.99 | 1.06	1.03 1.04	[49]
Silver oxide	Melt (C)		Zn: 1.03 | - O: 0.98 | 1.04	1.14 1.10	
Pd	HT (SPC)	E-beam evap.	O: - | 1.1 ± 0.1	$\sim$1	[44]
Ir	HT (TD)	E-beam evap.	Zn: 0.57 | -	3.5	[50]
Pd			Zn: 0.57 | 0.33	2.0	
Pt			Zn: 0.72 | 0.61	2.0	
Silver oxide			Zn: 1.00 | 1.05	1.06	
Au	VP (ZN)	Remote O_2/He plasma	Zn: 0.81 | 1.20 O: 0.77 | 1.07	1.2 1.3	[47]
Pd			Zn: 0.53 | 0.73 O: 0.61 | 0.68	1.3 1.2	

HT=Hydrothermal, TD=Tokyo Denpa Co. Ltd., C=Cermet Inc, SPC=SPC Goodwill, VP=Vapour phase, ZN=ZN Technology Inc.

3.5.2 ZnO/Si heterostructure

In 1994, Kobayashi *et al.* performed spray-pyrolysis of ZnO on Si to investigate the photovoltaic properties of this structure [51]. The films which were grown at 340 °C substrate temperature had sheet resistance of ∼300 Ω/□. The conversion efficiency reached 6.9 % with n-type Si, whereas the p-type Si substrate showed much lower efficiency. However, the performance of the cells was decreased or increased by exposure of UV for n-type and p-type substrate, respectively (see Fig.3.5). Supported by XPS results and

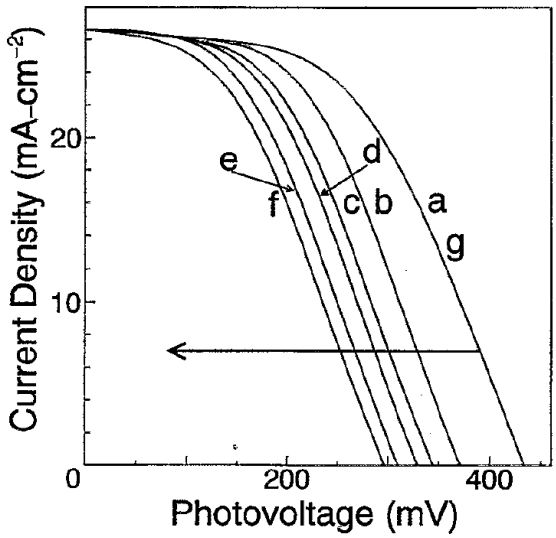

Figure 3.5: J-V curve of ZnO/n-Si under illumination. The light exposure time with AM1 is a) 0min, b) 3min, c) 6min, d) 20min, e) 70min and f) 120min, with UV-filter g) 120min. Figure adapted from Ref. [51].

investigations of the structure with an additional ITO layer, they argued that the work function of ZnO was modified by the desorption of O_2 in grain boundaries as EHP was generated in ZnO, and the desorption resulted in a change in the surface dipole moment. This behavior of oxygen adsorption/desorption was studied already in 1957 by D. A. Melnick [52].

RF magnetron sputtering for deposition of ZnO:Al on n-Si was performed by D. Song *et al.* [53] in 2002. The deposited films were optimized

in terms of argon pressure. With ZnO:Al film of $2.74\times10^{-4}\,\Omega$cm resistivity, an AM1.5[1] illumination measurement showed a conversion efficiency of 8.2%. No degradation was observed after a storage in air for three months, nor during a 2h illumination. Suggested by an earlier study [54], a suppression of oxygen diffusion was achieved through the dense structure of the films.

Motivated by the low-cost production method of sol-gel ZnO/n-Si solar cells, D. G. Baik *et al.* [55] investigated the performence of this cell with phosphorus surface doping of Si at 10^{20} and $10^{18}\,\mathrm{cm}^{-3}$ with/without SiO_2 as a passivation layer. The deposited ZnO-film had a sheet resistance of $100\,\Omega/\square$, and the best performance was obtained by high surface doping and a thermally grown oxide layer, yielding a conversion efficiency of 5.3% (see Fig.3.6).

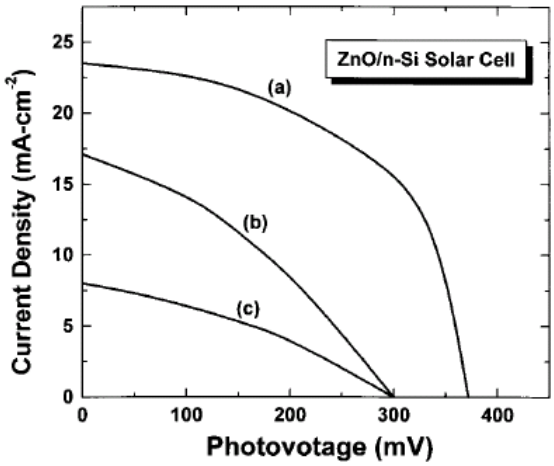

Figure 3.6: IV-curves of ZnO/n-Si under illumination. Effects of surface doping and oxide; a) SiO_2, $10^{20}\,\mathrm{cm}^{-3}$ b) SiO_2, $10^{18}\,\mathrm{cm}^{-3}$ and c) no SiO_2. Figure adapted from Ref. [55].

At this point, good photovoltaic behavior of ZnO/Si is only achieved

[1] AM - Air Mass represents the light spectrum that is received by a surface at sea level after modification by gasses in the atmosphere. '1.5' represents 1.5 atmosphere thicknesses, due to the angle of 48.2° between the outward normal of the earths surface and the sun (zenith angle).

with n-type Si. Althought a photocurrent is observed in revers bias for p-type Si, this current is significantly reduced in forward bias, which can be seen in the work by J. Y. Lee *et al.* [56]. They fabricated ZnO/p-Si structure by RF sputtering under various substrate temperature and Ar/O_2 ratio. The deposited films had a charge carrier concentration between 10^{16} to $10^{19}\,cm^{-3}$, confirmed by Hall measurements, and the IV-curves under illumination are shown in Fig.3.7. Similar studies were performed by W.

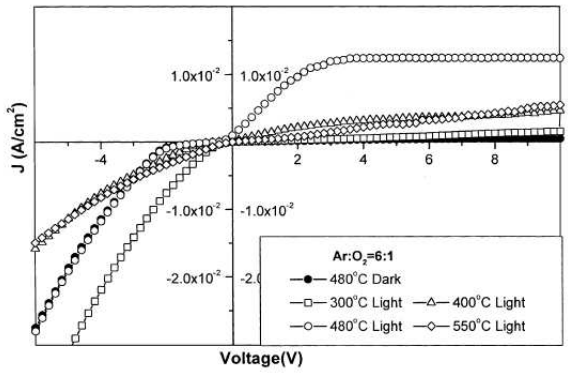

Figure 3.7: IV-curves of ZnO/p-Si under illumination for photodiodes fabricated in various substrate temperature. Figure adapted from Ref. [56].

Y. Zhang *et al.* in 2008 [57], which showed IV-curves of the same shape. Improvement of I_{SC} and V_{OC} were investigated via film thickness and oxygen partial pressure during DC sputtering. The behavior of I_{SC} as a function of oxygen partial pressure were discussed as an effect of mobility and charge carrier concentration due to intrinsic defect concentration in ZnO.

Chapter 4

Method and experimental techniques

In this chapter, the relevant simulation programs, experimental instruments and methods will be explained.

4.1 Sentaurus TCAD

The behavior of charge carrier in a device can be simulated using the formalisms described in Chapter 2. Several commercially available simulation software packages utilizing these equations in combination with finite element modelling exist. In the present thesis, the software TCAD from Synopsys has been used.

Sentaurus TCAD is a simulation tool which can solve fundamental physics equations, such as diffusion and transport, for thermal, electrical and optical devices. Primarely, this package is designed for Si technology, such that the material database and the parameters for physical models are related to Si-based devices. However, it allows a wide range of implementation and customization of user-defined material and physical models which is of benefits for the absence of parameter values valid for ZnO in the material database.

The developement of a ZnO model is performed by constructing ZnO-based devices with parameters taken from the literatures. The structural

models are then calculated to compare with experimental data, and thereafter adjusted and investigated for qualitative understanding of the physics behind the devices. This process involves modifications of the structural model and physical effects, which include the use of two programs within Sentaurus TCAD. A brief introduction of these two programs and the simulation methodology will be given.

4.1.1 The device structure

Geometrical structure of a device in two or three dimensions (2D/3D) is constructed using *Sentaurus Structure Editor* which supports graphical user interface (GUI) and command-line interface (CLI) [58]. A simulation structure with chosen materials, as well as user-defined materials, can be drawn in arbitrary shapes, referred to as regions (See Fig.4.1). These regions

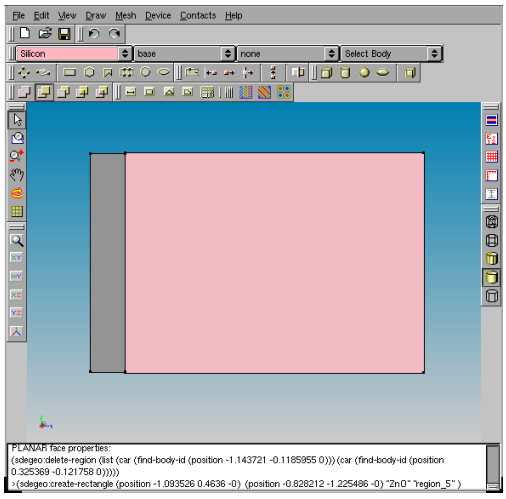

Figure 4.1: Graphical user interface of Sentaurus structure editor. A rectangular ZnO (grey) is drawn next to silicon (purple).

can then be implemented with doping material, concentration and profile, and/or connected to contacts for electrical and thermal simulations. As a requirement, a customized mesh with desirable range of density needs to

be added. An example of a command-file for Sentaurus Structure Editor can be found in Appendix B.1.

4.1.1.1 Structural design

All simulations performed in this work were drawn in 2D with a mesh accounting for only one axis. However, a thickness of 1 μm was assumed by the calculation program, which enabled the conversion of, for instance, current density.

Meshing of a device had most focused on the contacts and the junction where the physical quantities changed rapidly. This assured that physical effects which occured close to a junction, such as tunneling, were accounted for. The bulk region was kept with a much lower resolution to minimize the computational time. However, the mesh densities were examined for their accuracy by comparing a set of simulated results with different densities.

4.1.2 Simulating a device structure

Calculations of the pre-structured device are performed in *Sentaurus Device* , which is capable of calculating 1D, 2D and 3D devices for electrical, thermal and optical purposes [59]. The conditions for a simulation, such as physical models, mathematical interpretations and ramping parameters, are defined here. In addition, user-defined physical models (written in C++) can be implemented. The program also allows for *mix-mode* simulations with SPICE (Simulation Program with Integrated Circuit Emphasis). In this mode, circuits can be constructed, and alternating-current (AC) signals with desirable frequencies and amplitude are applied here to achieve capacitance-voltage (CV) and conductance-voltage (GV) curves. Local implementations are also available, to account for different quantities in heterojunctions, such that the band offsets and the band bending can be correctly calculated. An example of a command-file for Sentaurus Device can be found in Appendix B.2.

4.1.2.1 Simulation methodology

In all simulations, the electrostatic potential and the electron (hole) distribution in a device were calculated by solving the Poissons equation coupled with the continuity equation of electrons and holes. A strategy based on the global approximate Newtons iterative method by Bank and Rose (Ref. [60]) is utilized, in which the initial estimates was automatically generated by a built-in algorithm. The common physical models, such as doping dependent mobility, high field saturation and band gap narrowing were applied. Some other effects, such as tunneling, were examined individually as a variable.

In the absence of valid ZnO parameters in the material database, a user-defined parameter-file based on the literatures was created for this purpose, with the background structure of silicon. Thus, any unspecified parameters from this file came from the properties of silicon. The ZnO-parameters (recall Table 3.1) have large variations given from the literature, and finding the exact values by simulation is a challenging task, due to the large number of possibilities within one parameter. To reduce the number of variables, specific numbers for, e.g. mobility, effective mass etc. were taken from the literature (see Table 4.1). This will, of course,

Table 4.1: Simulation parameters for ZnO.

	Electron	Hole
Mobility $[cm^2/Vs]$	100	10
Effective mass $[m_*/m_0]$	0.28	0.59
Effective density of states $[cm^{-3}]$	$3.7 \cdot 10^{18}$	$1.1 \cdot 10^{19}$
Bandgap, $E_g(300K)$ [eV]	3.36 (direct)	
Relative permittivity $(E\|c)$, ϵ	8.91	
Electron affinity, χ [eV]	varied	

limit the quantitative agreement between simulations and experiments. On the other hand, the simulations can still give a good qualitative understanding of a situation. The electron affinity, which is a material specific parameter, is found to vary considerably in the literature (recall Tables 3.1

and 3.3). This quantity is important for determining the potential barrier experienced by charge carriers in a junction, which will result in different electrical characteristics. By varying this parameter and analyzing the simulated electrical characteristics, a deeper understanding of, not only, ZnO can be gained.

Sentaurus Device offers three mathematical methods to calculate the current density, which is by evaluation of either the whole device or vertices near the contacts. The latter option implies less accuracy due to the reliance on a small number of vertices. However, the former option, in some cases, gave non-physical results and large distortions. Therefore, the suitable method was chosen for one device after several tests. Otherwise, it has been noticed that all methods give the same current density.

4.2 Deep Level Transient Spectroscopy

Deep Level Transient Spectroscopy (DLTS) is a characterization method capable of determining energy level positions, concentration and capture cross-section of electrically active defects by sequential measurements of capacitance transients. This technique will be explained for a diode where the depletion region extends primarily into n-type material, e.g. p^+n-diode.

Principle

By changing the applied bias voltage over a junction, the depletion width varies between two spatial positions from the junction. As a consequence, trap states within this region will be occupied and emptied, and the effective doping concentration changes according to

$$N_{d,eff} = N_d - n_T, \tag{4.1}$$

where n_T is the concentration of trapped electrons. During the revers bias, the trapped electrons are re-emitted to the CB and n_T decreases as

$$n_T(t) = N_T e^{-e_n t}, \tag{4.2}$$

where N_T is the total concentration of the trap and t is the time. This change in n_T can be recorded by measuring the capacitance as a function of time, which is called the *capacitance transient*. To put words into formulas, recall the capacitance expression, Eq.(2.15), and substitute for the effective doping concentration, Eq.(4.1), one obtain:

$$C = \sqrt{\frac{q}{2\epsilon_r\epsilon_0(V_0 - V)}\,(N_d - n_T)}. \tag{4.3}$$

In the situation when $N_d \gg n_T$, the capacitance can be rewritten as[1]

$$C \approx \sqrt{\frac{qN_d}{2\epsilon_r\epsilon_0(V_0 - V)}}\left(1 - \frac{1}{2}\frac{n_T}{N_d}\right) = C_r - \Delta C(t), \tag{4.4}$$

where the capacitance transient,

$$\Delta C(t) = \frac{C_r N_T}{2N_d} e^{-e_n t}, \tag{4.5}$$

which relates the change in capacitance to the change in trap concentraition. The capacitance transient is recorded step-wise with a specific time-interval, τ, in between and a specific number of measurement depending on the *time-window* chosen. "Time-window i" corresponds to 2^i measurements.

A *DLTS signal*, S (usually normalized as S/C_r), is a mathematical interpretation of the capacitance transient in order to create a spectrum and to ease the handling of data. This is performed by applying a *weighting function*, w(t), on the capacitance transient

$$S_i = \frac{1}{2^i}\sum_{j=1}^{2^i} w(t_j)\Delta C(t_j) = \frac{C_0 N_T}{2N_d}\cdot\frac{1}{2^i}\sum_{j=1}^{2^i} w(t_j)e^{-e_n t_j} \tag{4.6}$$

with $t_j = 2^{j-1}\tau$, where t_j being the discretized time and i is the time-window. There are several different weighting functions available, one of which is the *Lock-in* function given as

$$w(t_j) = \begin{cases} 1 & \text{, for } 2^{i-1} < j \leq 2^i \\ -1 & \text{, for } 1 \leq j \leq 2^{i-1} \end{cases} \tag{4.7}$$

[1]Taylor series about x=0 for $\sqrt{1+x} = 1 + \frac{1}{2}x - \frac{1}{8}x^2 + ... = \sum_{n=0}^{\infty}\frac{(-1)^n(2n)!}{(1-2n)(n!^2)4^n}x^n$, for $|x| < 1$.

and schematically illustrated in Fig.4.2. More complicated weighting function, such as *GS4*, are able to distinguish adjacent defects levels on the expense of the signal to noise ratio.

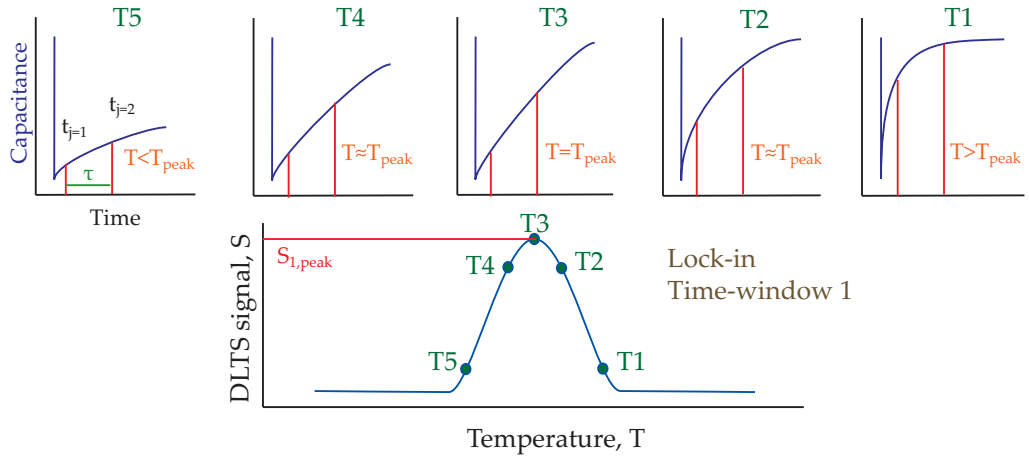

Figure 4.2: Capacitance transient at different temperature, i.e. different emission rate, and the corresponding points in the DLTS signal spectrum.

By having a specific time-interval, a certain emission rate will appear as a peak in the DLTS signal. Therefore, the choice of the time-window immediately provides a value for the exponential terms in the summation in Eq.(4.6). With a τ of 10 ms and lock-in weighting function, the summation at the DLTS peaks can be calculated, shown in Table.4.2.

Having the knowledge of the emission rate at several temperatures, the trap energy level and the capture cross-section can be obtained from a linear fit of the rewritten Eq.(2.38) in an Arrhenius plot

$$ln\left(\frac{e_n}{T^2}\right) = ln\left(\left[\frac{8\pi^{3/2}m^*k^2}{h^3}\right]\cdot\sigma_n\right) - \left(\frac{E_C - E_T}{k}\right)\frac{1}{T} \tag{4.8}$$

Here, an assumption of negligible ΔS and temperature independent capture cross section are made, where ΔS is the change in entropy. For further details, see Appendix A.1. The trap concentration is found from Eq.(4.6), given as:

$$N_T = \frac{2N_d S_{i,peak}}{C_0 F_i} \tag{4.9}$$

Table 4.2: The values of the summation in Eq.(4.6) with time-interval of 10 ms and lock-in weighting function and their corresponding emission rate at the peak.

Time-window i	$F_i = \frac{1}{2^i}\sum_{j=1}^{2^i} w(t_j)e^{-e_n t_i}$	$e_n\ [ms^{-1}]$
1	0.12488	36.2240
2	0.15489	22.7146
3	0.17597	13.1125
4	0.18880	7.13215
5	0.19594	3.73525
6	0.19971	1.91388
7	0.20165	0.969060
8	0.20264	0.489207

4.3 Admittance spectroscopy

Similar to DLTS, admittance spectroscopy (ADSPEC) is capable of determining energy levels, capture cross section and concentration of a defect. While DLTS requires low defect concentration compared to background doping, ADSPEC requires high defect concentration. Assuming only one donor level, this method will be explained. The representation of ADSPEC will follow that of Ref. [61].

Principle

The admittance is a quantity which is dependent on an AC probe frequency, and it is expressed with an in-phase and out-phase term:

$$Y(f) = G(f) + jS(f) \tag{4.10}$$

where $G(f)$ is the conductance, j is the imaginary unit and $S(f) = 2\pi f\, C(f)$ is the susceptance. As the doping concentration, N_D, is solely controlled by the trap concentration, which means $N_T = N_D$, the effective doping concentration becomes

$$N_{d,eff} = N_T(1 - e^{-e_n t}), \tag{4.11}$$

where t is the inverse measurement angular frequency, and the capacitance equation, Eq.4.3, changes accordingly.

When temperature reaches a certain value, characteristic to the donor, *freeze-out* of charge carriers occurs, which means that the defect no longer provide charge carriers to the CB and becomes neutral. The change in the charge carrier concentration as the temperature is lowered, will affect the capacitance and the conductance. By monitoring the development of these quantities in different temperature and frequencies, the donor characteristics are obtained.

As the temperature decreases and a defect level is freezing out, the capacitance falls to a value $C_{after} \approx 0$. The temperature corresponding to the midpoint value of C_{before} and C_{after} can also be observed as a peak in the G-T plot, shown in Fig.4.3. At that point, a ratio of the capacitances

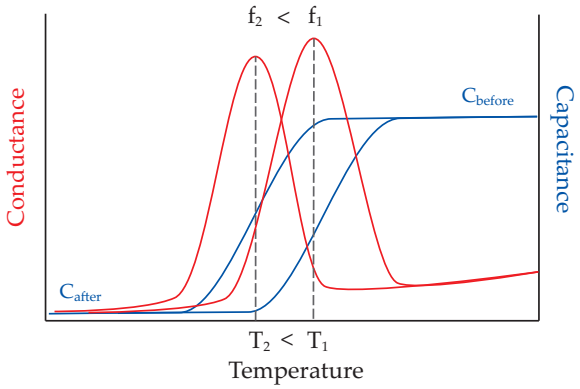

Figure 4.3: Schematical representation of the response in capacitance and conductance as a function of temperature for two different probe frequencies.

can be written as

$$\frac{C_{mid}}{C_{before}} = \sqrt{\frac{N_T(1 - e^{-e_n t})}{N_T}} = \frac{1}{2}. \tag{4.12}$$

Solving Eq.4.12 with respect to the emission, one obtains

$$e_n t = ln\left(\frac{4}{3}\right). \tag{4.13}$$

By recalling the emission rate as Eq.2.38, and preparing for an Arrhenius plot, the final expression becomes

$$ln\left(\frac{1}{T_p(f)^2 t(f)}\right) = ln\left(\left[\frac{8\pi^{3/2} m^* k^2}{h^3\ ln(4/3)}\right]\ \sigma_n\right) - \left(\frac{E_C - E_T}{k}\right)\frac{1}{T_p(f)} \quad (4.14)$$

This equation is similar to the one obtained for DLTS, and an evaluation of the gradient of the Arrhenius plot reveals the donor energy level position.

A more thorough description is required when evaluating a band gap with two or more defect levels. Although the defect concentration and the capture cross section will be affected by this formulation, the energy level position is still valid provided that the G-T peak is not shifted by an adjacent defect (due to overlap of peaks).

Chapter 5

Pd Schottky contacts to ZnO

In this chapter, preparation, measurement and simulation of palladium Schottky contacts and their results will be described and discussed. Experimental characterization was performed to investigate the conductivity and the nature of defects in ZnO to improve the simulation model for charge carrier transport.

5.1 Experiment

As-received ZnO wafers were hydrothermally grown by SPC Goodwill (Russia), with purity of $> 99.99\%$. These wafers were cut perpendicular to c-axis, with a size of 10x10x0.5 mm^3, and polished to a roughness of $R_a < 1.0\,nm$. The O-face [000$\overline{1}$] and Zn-face [0001] were recognized by the different cut at the corners (See Fig.5.1). The Table.5.1 shows the data sheet given by the supplier.

The as-received hydrothermal (HT) ZnO wafers were cut into four pieces shown in Fig.5.1. Two wafers, one initially high resistive (HR) and low resistive (LR), were chosen, with resistivity of 2100 Ωcm and 130 Ωcm, respectively, measured by 4-point probe method. One piece of each wafer were heat treated in air at temperatures of 1500 °C (labelled as HR-15 and LR-15) and 1200 °C (HR-12 and LR-12), and thereafter polished to remove the accumulation of defects and impurities at the surface caused by this treatment. These samples, along with two room temperature samples

Table 5.1: Properties of HT ZnO wafers provided by SPC Goodwill [62].

Electrical resistance	0.5-1 kΩ
Transmission (λ=400-600nm)	>50 %
Maximum transmission (λ=1200nm)	95 %
Specific heat	0.125 cal/gm
Thermal conductivity	0.006 $cal/(cmK)$
Thermoelectric constant (T=573K)	1200 mV/K
Bandgap (T=298K)	3.37 eV
Exciton binding energy	60 meV
Etch channel density	100 pcs/cm^2

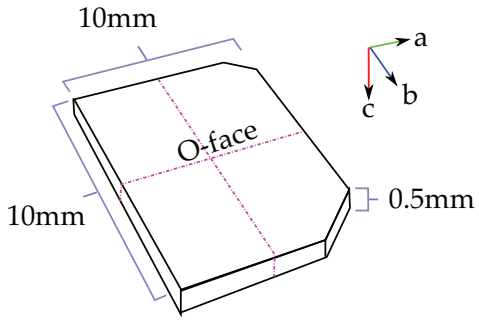

Figure 5.1: Hydrothermal ZnO wafer cut into 4 pieces.

(HR-RT and LR-RT) were treated with aceton, ethanol and hydrogen peroxide in total of 15 min before deposition of Pd for Schottky contacts, using an e-beam evaporator, through a shadow mask with hole diameters of 0.3 mm, 0.5 mm and 0.8 mm. The base pressure before commencing the deposition was $\sim 10^{-7}$ mbar and the deposition rate varied between 0.2 Å/s to 0.4 Å/s. A thickness of 100 nm Pd, confirmed by the quartz crystal within the e-beam chamber, was deposited on the ZnO O-face. A post-annealing at 200 °C for 30 min was performed before the electrical characterizations with DLTS and ADSPEC, current-voltage (IV) and capacitance-voltage (CV) measurements. Silver paste[1] was used as the back-contact.

[1]Silberleitlack Art-Nr: 530042, Germany

The chart flow of the experiment is shown in Fig.5.2.

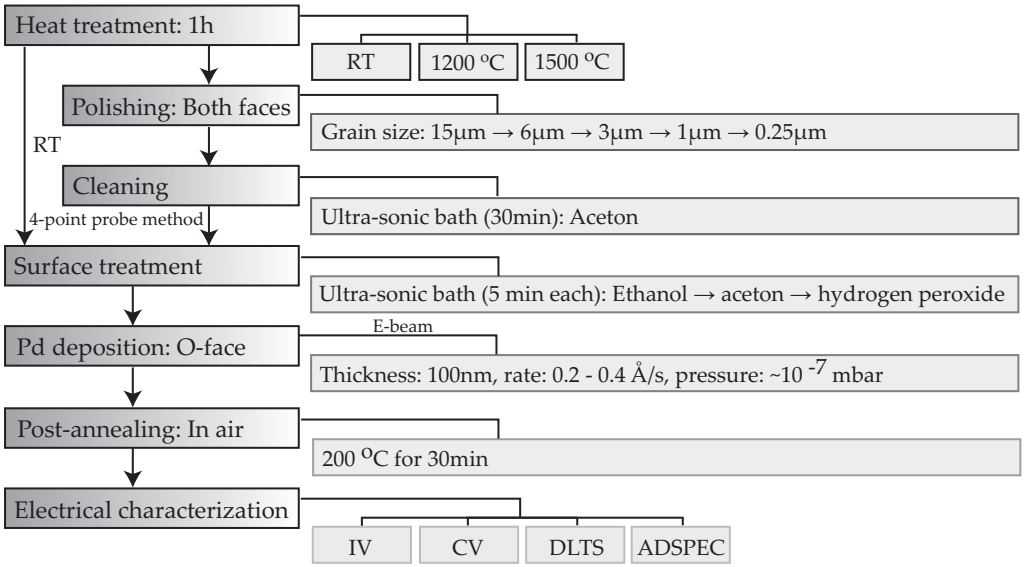

Figure 5.2: Chart flow for the preparation of Pd Schottky contact.

5.1.1 Experimental results and discussion

Resistivities

Confirmed by the 4-point probe method, the resistivities were observed to decrease by up to 4 orders of magnitude after heat treatment, with the lowest resistivity of 0.13 Ωcm which coincided for both wafers (HR and LR). Assuming dominant n-type conductivity, mobility of 100 cm^2/Vs and effective density of states for electron of 3.7×10^{18} cm^{-3}, the corresponding carrier concentrations and Fermi-level below CBE were calculated with Eq.2.1 and Eq.2.5 (see Table.5.2).

The reduction of resistivity by heat treatment was also observed in the work by Maqsood [25], where it was suggested a relation with the decrease in lithium concentration. Since Li is proposed as a compensating impurity, removal of Li will increase the free charge carrier concentration.

Table 5.2: Resistivities, carrier concentration and Fermi-level for initially high and low resistive wafers after heat treatment in RT, 1200 and 1500 °C.

Wafer, HR	RT	1200 °C	1500 °C
Resistivity [Ωcm]	2.10×10^3	6.2	0.13
n [cm^{-3}]	3.0×10^{13}	1.0×10^{17}	4.8×10^{17}
$E_C - E_F$ [eV]	0.30	9.3×10^{-2}	5.3×10^{-2}
Wafer, LR	RT	1200 °C	1500 °C
Resistivity [Ωcm]	1.3×10^2	3.3	0.13
n [cm^{-3}]	4.8×10^{14}	2.0×10^{17}	4.8×10^{17}
$E_C - E_F$ [eV]	0.23	7.6×10^{-2}	5.3×10^{-2}

IV-characteristics

The IV-curves with the highest rectification, here defined as I(1V)/I(-1V), for different samples are plotted in Fig.5.3. A trend of lower rectification and higher leakage current is seen in LR with increasing heat treatment. However, the same trend is not followed by HR. Here, the leakage current remains fairly stable, while the forward bias is increased by increasing temperature treatment, which shows an improvement of contacts.

It should be mentioned that the contact reproducibility was very low, where the rectification varied by up to 3 orders of magnitude on the same sample with various leakage currents. In addition, this rectification quickly degraded by time, and became nearly Ohmic after 1-2 weeks for the heat treated samples. The untreated samples had contacts decaying only sligthly (maximum 1 order of magnitude) after a month, which suggests that either the heat treatment or the polishing affects the contact stability.

Series resistance, R_s, and ideality factor, η

In order to obtain the value of ideality factor, the series resistance had to be known. Utilizing the current density equation, Eq.2.5, from the thermionic emission theory, the series resistance was found by plotting $\frac{1}{I}\frac{dI}{dV}$ versus $\frac{dI}{dV}$ and evaluating the linear fitting of the curve in the range where the R_s

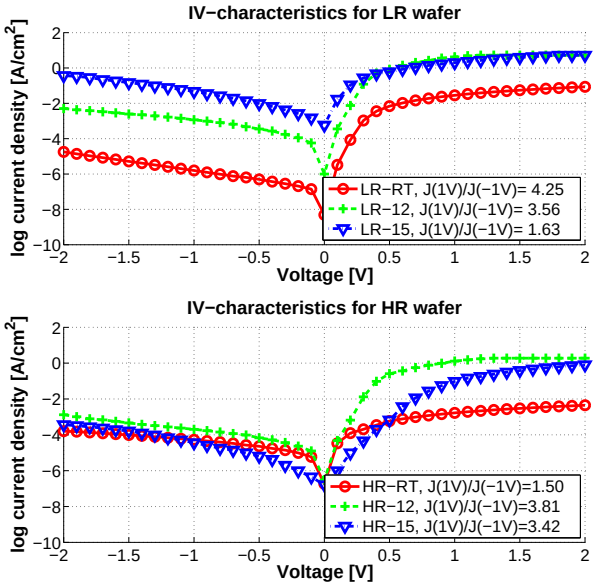

Figure 5.3: IV-curves with the highest rectification obtained from Pd Schottky contact on HR and LR ZnO under various heat treatment.

dominated ($V \geq 1.0\,\mathrm{V}$). However, due to instrumental limitation of current (I_{max} ~3.7 mA), large standard deviation is observed (see Table.5.3).

Table 5.3: The calculated series resistances for the IV-curves shown in Fig.5.3, with standard error.

Series resistance, R_s	RT	1200 °C	1500 °C
HR [Ω]	$(5.1 \pm 0.3) \times 10^4$	$(8.0 \pm 1.6) \times 10^2$	$(4.3 \pm 3.0) \times 10^2$
LR [Ω]	$(6.5 \pm 1.3) \times 10^3$	$(1.6 \pm 0.6) \times 10^2$	$(1.5 \pm 0.5) \times 10^2$

The ideality factor was then calculated with the estimated series resistances and showed a value of 1.06±0.03 in revers bias (see Fig.5.4). However, this factor rapidly increased in forward bias, suggesting that the ideal carrier transport was altered by carrier recombination, tunneling and/or an interfacial layer.

By utilizing the same equation, the barrier height was calculated for

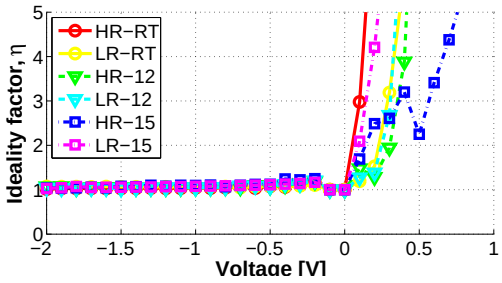

Figure 5.4: Ideality factors for the IV-curves obtained in Fig.5.3.

large revers bias, obtaining $\Phi_{b,IV} < 0.32\,\text{eV}$, which is far lower than the previously reported values obtained from IV-curves (recall Table.3.3). The low barrier height reflects presumably the presence of substantial tunneling and/or interface traps.

CV-characteristics

The capacitance of the Pd Schottky contacts is dependent on the charge carrier concentration in ZnO, given in Eq.2.15. Judged by the 4-point probe measurements, the capacitances should increase with higher temperature treatment, which was indeed the case for LR (see Fig.5.5). However, this trend was not followed by HR-12 and HR-15 which had the same contact size. In addition, a similar value for the capacitance is expected between HR-15 and LR-15, due to approximately the same charge carrier concentration. Assuming that the bulk charge carrier concentration is uniformly distributed, the variations in the capacitances could indicate effects from the interface.

By evaluating the linear fit of $\frac{1}{C^2}$ versus V, the barrier height and the charge carrier concentration could be deduced. Both HR/LR-15 and HR/LR-12 were evaluated with charge carrier concentration of $1.5 \pm 0.5 \times 10^{17}\,\text{cm}^{-3}$, which agreed well with the values in Table.5.2. Using Eq.2.19, the barrier heights were calculated with the lowest value of 1.2 eV (LR-15) in the range between 0 V to 0.5 V, which coincides with the highest reported ones in the literature.

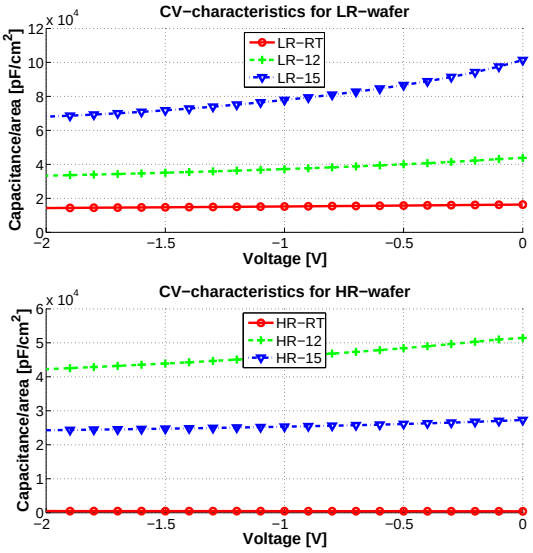

Figure 5.5: The corresponding CV-curves to Fig.5.3.

Deep level traps from DLTS

Due to the high resistivity in the RT samples, a complete freeze-out of charge carriers was reached already at 230 K. Thus, DLTS was unable to uncover any defect levels below that temperature for these samples.

The DLTS spectra obtained for all heat treated samples are plotted in Fig.5.6, where three peaks are visible, showing deep levels of 0.19, 0.31 and 0.57 eV below CBE. The commonly observed level at 0.31 eV is usually referred to as E3 in the literature. No distinction between HR and LR can be seen by the defects. For the wafers heat treated at 1200 °C, the defect level at 0.19 eV was observed with concentration of $5 \times 10^{15}\,\mathrm{cm}^{-3}$ and capture cross section of $1.5 \times 10^{-16}\,\mathrm{cm}^2$, calculated by Eq.4.9. The same peak is assumed to be present in HR. The noise in the measurement is due to freeze-out of charge carriers, which is indicated by the revers bias steady-state capacitance (not shown). The energy position of the defect level after heat treatment at 1500°C, was extracted to be 0.57 eV below CBE with concentration and capture cross section of $1.4 \pm 0.3 \times 10^{15}\mathrm{cm}^{-3}$ and $3.5 \pm 1.5 \times 10^{-13}\mathrm{cm}^2$, respectively.

Attempts were made on finding a more accurate capture cross section

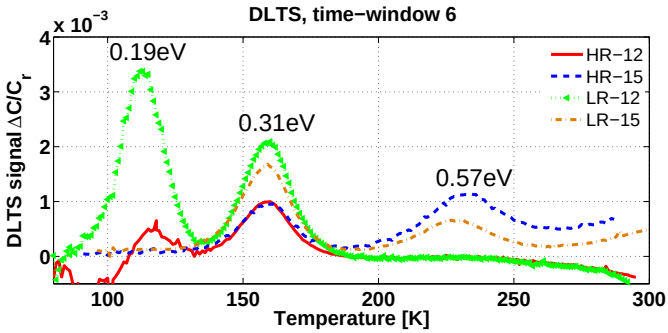

Figure 5.6: DLTS signals, with time-window 6, showing characteristic peaks after heat treatment.

by varying the width of the filling pulse while keeping the same revers bias. The obtained plot of DLTS signal versus filling pulse width was compared with the model given as (Ref. [63])

$$N_T^- = N_T(1 - exp(-c_n n t_p)), \tag{5.1}$$

where N_T^- is proportional to the DLTS-signal, N_T is the trap concentration, t_p is the pulse width and c_n is the capture cross section for electrons defined in Eq.2.31. However, the obtained curves were strongly dependent on the amplitude of both the revers bias and filling pulse height, and the fitting of these curves gave large uncertainties.

Shallow level traps from ADSPEC

Figure 5.7 shows the conductance (5.7*a*) and capacitance (5.7*b*) as a function of temperature for the heat treated samples, measured with AC frequency of 1 MHz. For all the samples, one major defect level, the freeze-out level is observed. The defect levels observed dependend both on wafer and temperature treatment, with the most shallow levels found in the HR/LR-15 samples. However, to uncover the most shallow defect levels, a temperature much lower than 20 K was required. This could not be reached with our cryostat. On the other hand, the defect levels for HR-12 and LR-12 were found at 0.060±0.005 eV and 0.030±0.003 eV below

a)

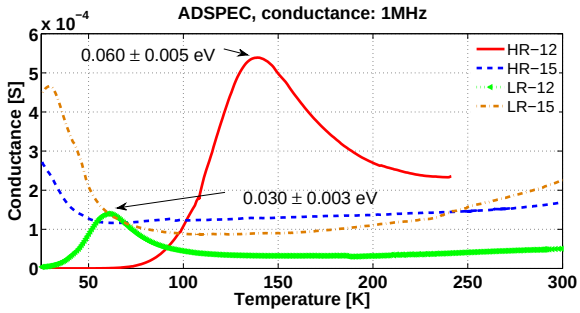

b)

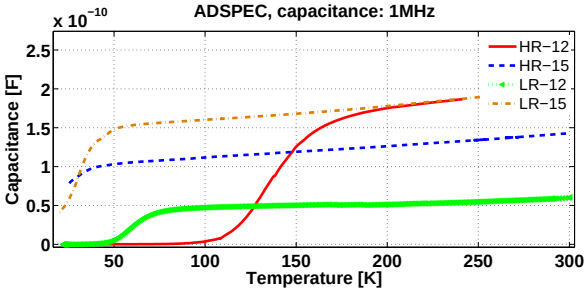

Figure 5.7: C-T and G-T from ADSPEC measurement for different heat treated wafers, which shows characteristic peaks from HR and LR.

CBE, respectively. Since these defects result in a complete freeze-out of charge carrier in the samples, the concentration is assumed to be given by the capacitance measurements previously discussed ($\sim 10^{17}\text{cm}^{-3}$). The capture cross section associated to the '0.06eV' and '0.030eV' peaks was $1.3 \times 10^{-17}\text{cm}^2$ and $5.8 \times 10^{-17}\text{cm}^2$, respectively, based on Eq.4.14.

5.2 Simulation methodology and parameters

A ZnO material database was developed for Sentaurus TCAD charge carrier simulations based on the literature data as described in Chapter 4.1. In order to improve this database for ZnO based device simulations, and to investigate the Schottky-barrier behavior in ZnO, a model was developed for comparison with the electrical measurements.

A 500 μm ZnO quasi-one-dimensional Schottky structure was defined with non-material-specified contacts at each end (see Fig.5.8). The Pd electrical property was later assigned for one of the contact in the Sentaurus Device with work function of 5.12 eV, and thus the model was independent of the contact thickness. Electrically, this design is valid because the metal has much lower resistivity than the semiconductor. Since the investigation of this structure was focused on the effect of traps, the electron affinity of ZnO (χ_{ZnO}) was set to 4.1 eV, which is approximately the mid value of the reported electron affinities for ZnO in the literature.

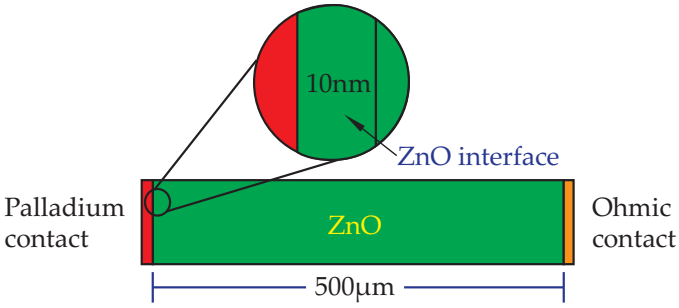

Figure 5.8: A schematical figure of the simulated structure, consisting of a 10 nm interface region and a bulk region of ZnO.

Motivated by experimental results, three trap levels were implemented with concentrations and energy levels shown in Table 5.4. However, the electron concentration in ZnO was entirely controlled by the shallow level (N_{D1}), due its high concentration and level close to CBE.

Interface trap was implemented as a level and placed 0.1 eV below (above) the CBE (VBE) for donor (acceptor) traps. The interface trap is mainly meant to provide a change in the charge carrier concentration and

Table 5.4: Parameters suggested by experimental results for the bulk region. Units are $[cm^{-3}]$ for concentration N, $[eV]$ for energy E and $[cm^2]$ for capture cross section CC.

E_{D1}	N_{D1}	CC_{D1}	E_{D2}	N_{D2}	CC_{D2}	E_{D3}	N_{D3}	CC_{D3}
0.03	10^{17}	10^{-17}	0.19	10^{15}	10^{-16}	0.31	10^{15}	10^{-15}

thus the energy level distribution (delta function) and its position are chosen only for the purpose of investigation. Due to software limitations on interface traps adjacent to a contact, a 10 nm defect rich layer of ZnO was created between Pd and bulk ZnO (see Fig.5.8). This depth length was also motivated by the extension of the near-surface layer affected by the hydrogen peroxide treatment, Fig.3.4.

Beside the aforementioned physical model in Section 4.1.2, image force was added to the Schottky contact. The effective barrier height is described as $\Phi_{B,eff} = \Phi_B + \Delta\Phi_B$, with

$$\Delta\Phi_B(F) = a_1 \left[\left(\frac{F}{F_0} \right)^{p_1} - \left(\frac{F_{eq}}{F_0} \right)^{p_1} \right], \tag{5.2}$$

where $a_1 = 2.6 \times 10^{-4}$ eV, $p_1 = 0.5$, $F_0 = 1\,\mathrm{V/cm}$, F is the electric field and F_{eq} is the equilibrium electric field in order to obtain $\Delta\Phi_B = 0$. These are the default values.

Sentaurus Device can incorporate tunneling models in several ways. A recommended and sophisticate method is called *non local tunneling* (NLT). As in other methods, it requires the specification of tunneling masses for electrons and holes, which are unknown. Thus, these quantities also became a variable in the search for a good fitting between experimental and simulated results. NLT is based on the work by Ieong *et al.* [64], but, with significant enhancements [59] (p.425).

5.2.1 Simulation results and discussion

Ideal Schottky contact

The ideal IV-characteristic, i.e. no interface trap or tunneling, gave a higher forward and lower revers current density compared to the experimental results, and it showed a rectification of 11 orders of magnitude, see Fig.5.9. As seen in Eq.2.24 and 2.23 for the current density, revers bias is controlled by the difference between the metal work function and the electron affinity of the semiconductor, i.e. the barrier height. The larger leakage

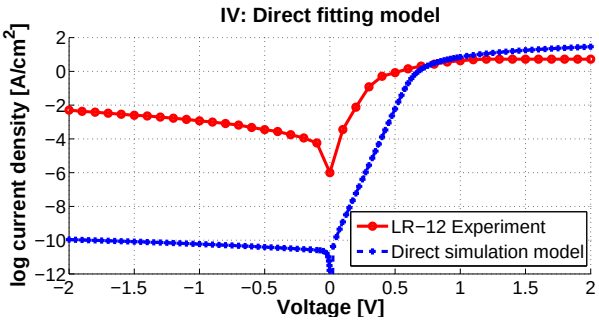

Figure 5.9: Fitting of experimental result by direct model. No interface trap or tunneling applied.

current in the real diodes compared to the simulations indicates a lower effective barrier height. However, bearing in mind the uncertainties in χ_{ZnO}, an increase of 0.1 eV in χ_{ZnO} will increase the current density by $log\left[exp\left(\frac{q\Delta\Phi_B}{kT}\right)\right] \approx 1.67$ orders of magnitude, which affects *all* contacts.

The saturation during a large forward bias is an effect of the series resistant. A lower experimental current density can also be caused by contact resistance. However, the numerical fittings are focused on the revers bias.

Interface traps

For interface trap concentrations of $5 \times 10^{12}\,\mathrm{cm}^{-2}$ in the interface region, the general effects on the band diagram are shown in Fig.5.10. Variations in potential barrier and depletion width can be observed, where the latter follows qualitatively the expression given for the depletion width in Eq.2.12.

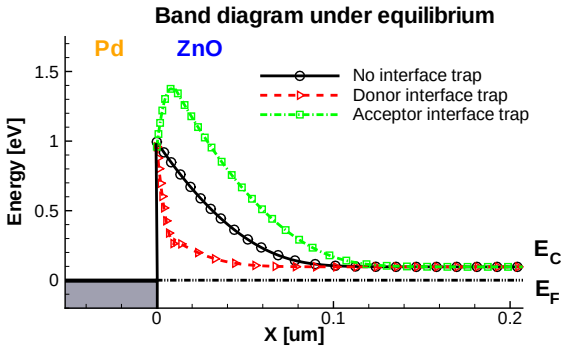

Figure 5.10: Band diagram at equilibrium for no interface trap, donor interface trap and acceptor interface trap.

As the potential barrier is increased for an acceptor interface trap, leakage current is decreased, giving rise to an even higher rectification (see Fig.5.11). In addition, a larger depletion width will reduce tunneling (although not applied here) from Pd to ZnO, which is undesirable in the search for higher leakage current. Thus acceptor interface trap is discarded in further discussion.

The donor (and acceptor) interface trap affects the potential barrier by band gap narrowing (due to high concentration), which in turn increases the electron affinity. However, this effect is minor ($\Delta\chi = 0.036\,\text{eV}$), and will not influence the results significantly.

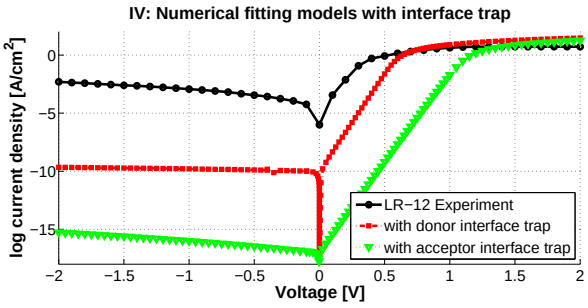

Figure 5.11: Fitting of experimental results, including interface trap.

Tunneling and donor interface traps

As mentioned previously, tunneling masses were investigated as a variable parameter. Through IV-curves, these masses were judged by the most likely shape and magnitude in the revers bias by comparison with experimental results. The chosen values for the electron and hole tunneling mass were 0.1 m_0.

The combined investigations of tunneling and interface trap on leakage current are summerized in Fig.5.12. Investigating the revers bias, an interface trap concentration larger than $10^{12}cm^{-2}$ is sufficient to have an increasing impact on the leakage current, which is within the thermionic field emission region ($10^{18}cm^{-3}$). As the concentration reaches

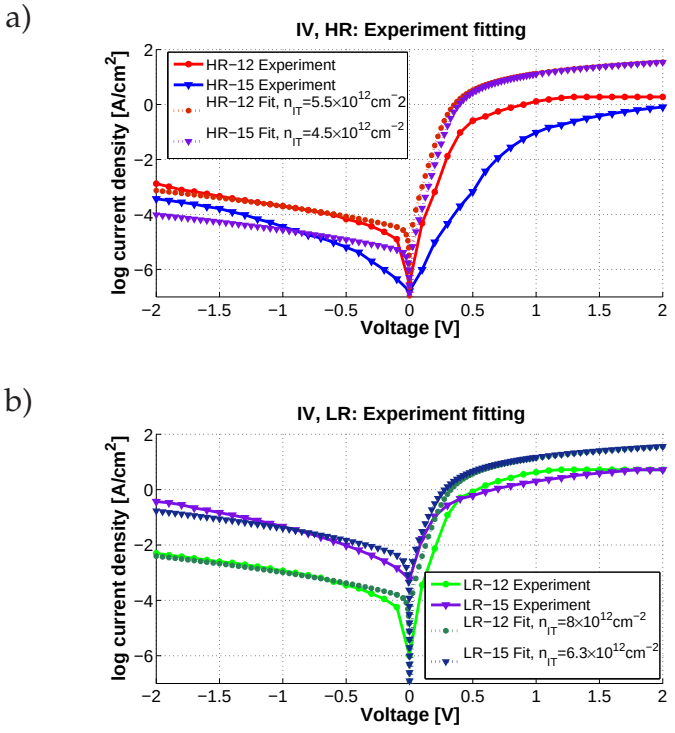

Figure 5.12: IV-fitting of experimental results, including interface trap and tunneling.

$4.5 \times 10^{12}cm^{-2}$, the revers current passes HR-15, but the fitting has large

deviations (see Fig.5.12*a*). However, requiring only small adjustments to the interface concentration, with intervals of around 10 factors of bulk concentration, other experimental results are fitted within small errors. This shows the large effect on diode performance by small changes in the interface trap concentration, which can exist between contacts on the same sample. In addition, due to the high solid solubility of hydrogen in palladium, it suggests that indiffusion of hydrogen can increase the donor concentration at the interface and/or passivate acceptor states, resulting in a degradation of diode performance by time, in agreement with Y. Dong *et al.* [47].

CV-curves corresponding to the simulated IV-curves in Fig.5.12 are shown in Fig.5.13. Although the values of the capacitance are of the same orders of magnitude, the gradients are highly mismatched. Moreover, the simulated capacitance is significantly larger than the experimental one in low revers bias, which means that the depletion width is smaller, indicating an overestimated charge carrier concentration. Comparing the distances between the interfacial layer and the depletion width, the large gradient at small reverse bias is believed to be caused by the interfacial layer as the majority carrier concentration is large and decreasing rapidly. Reducing this concentration gradient requires an increase or decrease in the bulk or interface doping concentration, respectively. However, this will also increase the saturation current in forward bias or decrease the leakage current. This only illustrates that the simplicity of this model is not sufficient to give detailed explanation for the real diodes.

Improvements of the model can be made by investigating the effect of interface traps with various energy posistions and depth profile in addition to the thickness of the interface layer. Moreover, additional layers can be implemented to account for defects which are induced in the wafers by polishing [65].

a)

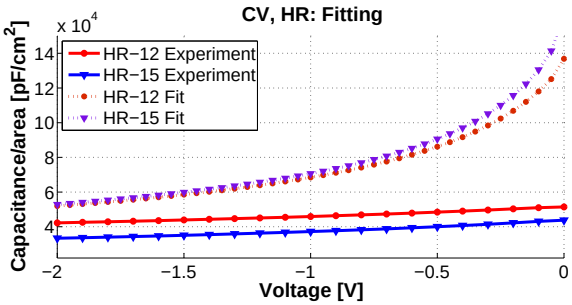

b)

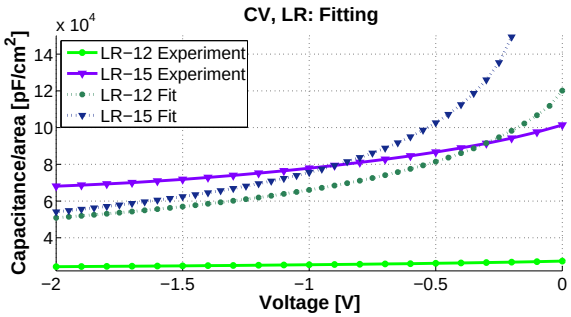

Figure 5.13: Corresponding CV-curves for the IV-fittings in Fig.5.12.

Chapter 6

ZnO/Si heterostructure

As discussed in the introduction, ZnO is interesting as a TCO for solar cell applications. Therefore, based on the experimental findings and the models developed in Chapter 5, a ZnO/Si heterostructure is explored in the present chapter.

6.1 Simulation methodology and parameters

The model structure consisted of a 100 nm region of ZnO followed by a 500 μm region of Si, where Ohmic contacts were applied to both ZnO and Si (see Fig.6.1). Simulations were performed to investigate the band diagram, IV-characteristics and charge carrier transport through various conditions, such as under illumination and with interface traps present. Material variations were focused on the electron affinity of ZnO (χ_{ZnO}), doping concentration in ZnO and doping type of Si (see Fig.6.2). The variation of χ_{ZnO} (from 3-5 eV) provided simulations of Type I and Type II heterojunctions ($\chi_{Si} = 4.05$ eV and $E_{g,Si} = 1.1$ eV), and it was motivated by the large uncertainties in the literature. As observed in the previous simulations, the shallow levels were fully ionizied and acted similar to doping. Thus, in the following simulations, the charge carrier concentrations are implemented as doping instead of a defect with specific energy level.

Illumination was provided by one wavelength of energy of 2 eV us-

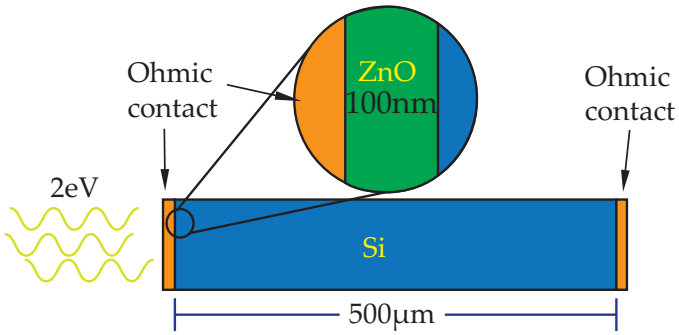

Figure 6.1: Simulation structure for ZnO/Si heterostructure.

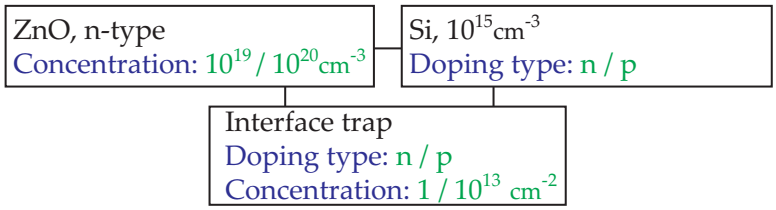

Figure 6.2: Combination diagram

ing a power density of 2.9 mW/cm^2, which corresponds to AM1.5. As the energy was less than the band gap of ZnO, ZnO was considered as completely transparent, while the absorption coefficient of Si was $\sim 4.5 \times 10^3\,\mathrm{cm}^{-1}$. As in the simulations for the Schottky contacts, the interface traps were implemented as acceptors or donors with energy level of 0.1 eV below/above its corresponding band of ZnO ($E_D = E_C - 0.1eV$ and $E_A = E_V + 0.1eV$) with a density of $10^{13}\,\mathrm{cm}^{-2}$. Having the mesh length of $\sim$0.7 nm at the interface, the trap density is equivalent to a concentration of $\sim 10^{20}\,\mathrm{cm}^{-3}$, which is higher or comparable to the bulk doping concentration. Tunneling is also implemented with parameters obtained from previous simulations. The cathode was put on the Si-side.

6.2 Results

The results will be divided into two main parts, consisting of *i*) *n*-ZnO/p-Si and *ii*) n-ZnO/*n*-Si. In each part, simulations with/without interface trap and/or illumination will be given in turn, begining with the most ideal case, i.e. no interface trap and no illumination. An overall discussion of the results is found at the end.

6.2.1 n-ZnO/p-Si

6.2.1.1 n-ZnO/p-Si: Band diagram

The simulated band diagram for n-ZnO on p-Si with different χ_{ZnO} is shown in Fig.6.3, where Si is located to the left of the junction at -0.1 (abscissa). The lowest part of VB_{ZnO} in Fig.6.3*a* is omitted to increase the readability, and Fig.6.3*b* shows the details of the CBE near the junction. Due to the high doping concentration in ZnO ($n_{D,ZnO}$) of $10^{19}cm^{-3}$, the Fermi-level of ZnO ($E_{F,ZnO}$=0) crosses the CBE_{ZnO} by 0.05 eV according to the diagram.

a)

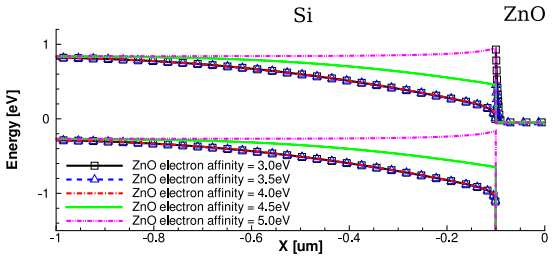

b)

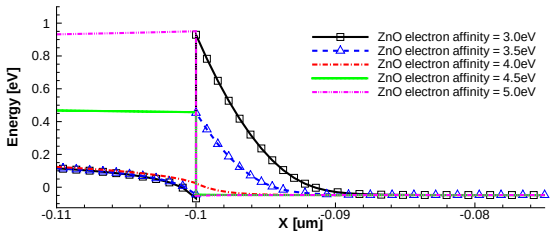

Figure 6.3: The band diagram for n-ZnO/p-Si, the VB_{ZnO} is omitted to increase the readability. a) Shows the band bending. b) Shows the CBE near the junction.

It can also be observed that the band alignment in Si follows approximately the same way for $\chi_{ZnO} \leq 4.0$ eV, hereafter abbreviated $\chi_{\leq 4.0}$, where the conduction band of ZnO (CB_{ZnO}) bends strongly to meet the Fermi-level of Si ($E_{F,Si}$) creating a "spike". A way to explain this behavior is to state that the "limit" of band bending in Si is reached. Physically, lifting up $E_{F,Si}$ requires charge compensation in a large depletion width which is provided by a narrow region in ZnO (due to doping concentration differences). The ratio between these distances are kept constant, but the transfer of charge carriers is increasing exponentially with Fermi-level. Thus, in order to increase $E_{F,Si}$ slightly near the CBE, a large decrease in Fermi-level in ZnO is required.

Band diagrams for different electron affinities and applied voltages are shown in Fig.6.4, where $\chi_{3.5}$ is omitted due to similarities to $\chi_{3.0}$ and $\chi_{4.0}$, and the "spike" in $\chi_{3.0}$ can again be seen. The effect of revers and forward bias are observed as lifting and lowering of the CBE of Si, respectively. Besides in the case for $\chi_{5.0}$, the CBE of ZnO is only slightly affected. It should be noted that the band bending in Si turns from downward to upward bending (disappearance of depletion region) in $\chi_{\geq 4.5}$ with increasing bias. The consequences will be highlighted in IV-characteristics.

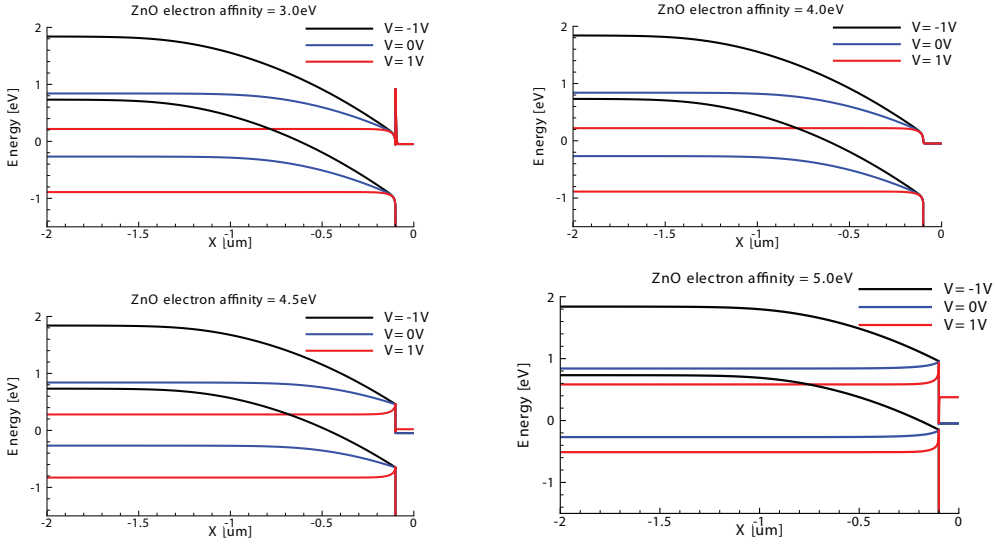

Figure 6.4: Band bending under applied voltage for various χ_{ZnO}

6.2.1.2 n-ZnO/p-Si: IV-characteristics

Three typical IV-curves can be extracted from the band diagrams in Fig.6.4, where curves having $\chi_{\leq 4.0}$ are very similar (see Fig.6.5). Comparing curves having $\chi_{\leq 3.5}$ with $\chi_{4.0}$ indicates that the thin barrier in ZnO is virtually non-existing due to tunneling.

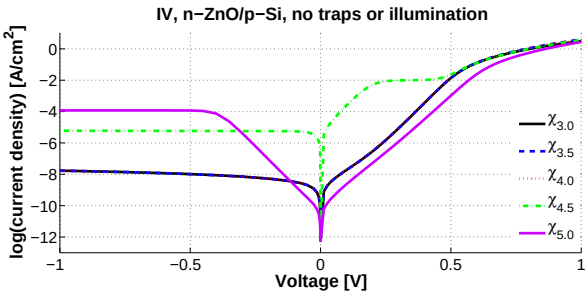

Figure 6.5: IV-characteristics for the chosen χ_{ZnO}.

A shoulder is present in the curve with $\chi_{4.5}$, where the current rises again at forward bias of $\sim$0.3 eV. By closer inspection of the band diagram, this happens in the transition between downward and upward bending of CB_{Si}. To investigate this shoulder even further, simulations of various electron affinity around $\chi_{4.5}$ was performed, see Fig.6.6. The observed

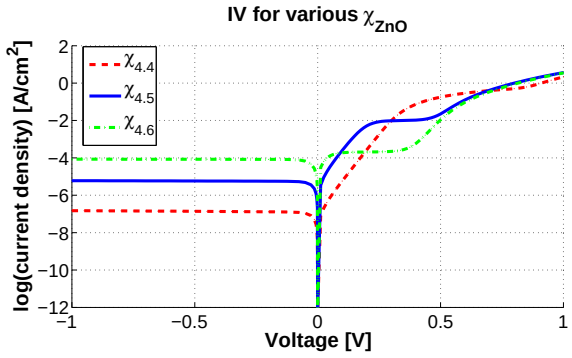

Figure 6.6: IV-characteristics of n-ZnO/p-Si with various χ_{ZnO} around $\chi_{4.5}$, i.e. $\chi_{4.4}$ and $\chi_{4.6}$.

effects were that the shoulder changed by $\sim$1.67 orders of magnitude cor-

responding to $\Delta\chi = 0.1\,\text{eV}$, while the potential barrier from ZnO to Si remained the same. This phenomenon can thus be explained by splitting the potential barrier, into two, the band offset and the band bending in Si (see Fig.6.7). When a low voltage is applied, Fig.6.7*a*, electrons from ZnO

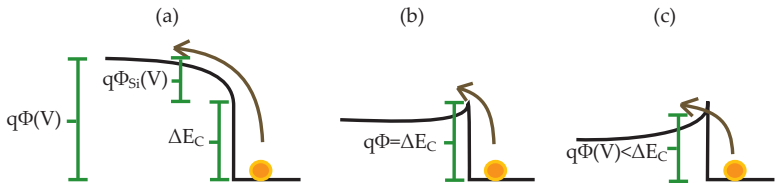

Figure 6.7: Carrier transport at different stages in the IV-curve during forward bias, where electrons from ZnO surmount a potential barrier set up by a) the band offset and band bending and b) the band offset by thermal excitation and c) by tunneling.

overcome the potential barrier by thermal excitation, which is exponentially dependent on the voltage. However, at the point when the depletion region disappears, Fig.6.7*b*, the electrons will experience the voltage independent barrier ΔE_C until tunneling starts to happen, Fig.6.7*c*.

The linearity (in logaritmic plot) in $\chi_{5.0}$ is due to band-to-band tunneling. Since the distance between VB_{Si} and CB_{ZnO} is fixed, a large forward bias results in ZnO conduction band lifting where charge transport mainly occurs in the CB. The current during revers bias becomes saturated because of limited minority carrier in Si going to ZnO.

6.2.1.3 n-ZnO/p-Si: Illumination

Figure 6.8 shows the simulated IV-curves when illumination is applied. As expected, the IV-curves for the ZnO models remain equal for $\chi_{\leq 4.0}$, and the current developement follows the process decribed in Section 2.2.7. This development is also found in the IV-curve with $\chi_{4.5}$, however, with a lower V_{OC} which can be explained by the higher dark current (current without illumination). The curve for $\chi_{5.0}$ does not follow the simple relation expected from Section 2.2.7, where two shoulder can be seen. The unusual

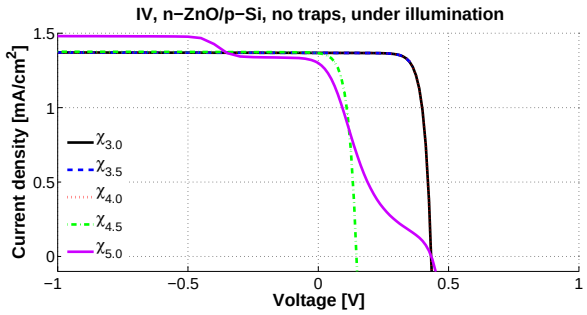

Figure 6.8: IV-characteristics of n-ZnO/p-Si under illumination with $E = 2\,\text{eV}$ and a power density of $2.9\,\text{mW/cm}^2$.

shape of $\chi_{5.0}$ can be explained through the band diagram. The current drop in revers bias (at $\sim$0.3 V) coincides with the transition *from upward* to downward bending of Si (recall Fig.6.4). For that reason, it is believed that the electric field is causing this effect. Although the electric field becomes unfavorable for photocurrent, the remaining current in forward bias is believed to be caused by charge carrier gradient (from equilibrium) and tunneling of photogenerated EHP. Since the potential barrier in Si changes only slightly as the CB of ZnO lifts up, a second graded shoulder occurs.

With this np-junction, the highest conversion efficiency is reached for $\chi_{\leq 4.0}$ with $\eta \approx 15.9\%$ with $V_m \approx 0.36\,\text{V}$ and $I_m \approx 1.27\,\text{mW/cm}^2$.

6.2.1.4 n-ZnO/p-Si: Interface trap

As the donor concentration in ZnO is already quite high, a donor rich region at the interface gives similar results, except for a slightly higher recombination rate, which is also present with acceptor interface traps. Thus, simulations with donor interface traps will not be regarded any further.

On the other hand, an interface with an acceptor trap density of $10^{13}\,\mathrm{cm}^{-2}$ modifies the band diagram significantly, see Fig.6.9, and IV-characteristics change accordingly, as shown in Fig.6.10. The IV-curves for low χ_{ZnO} dif-

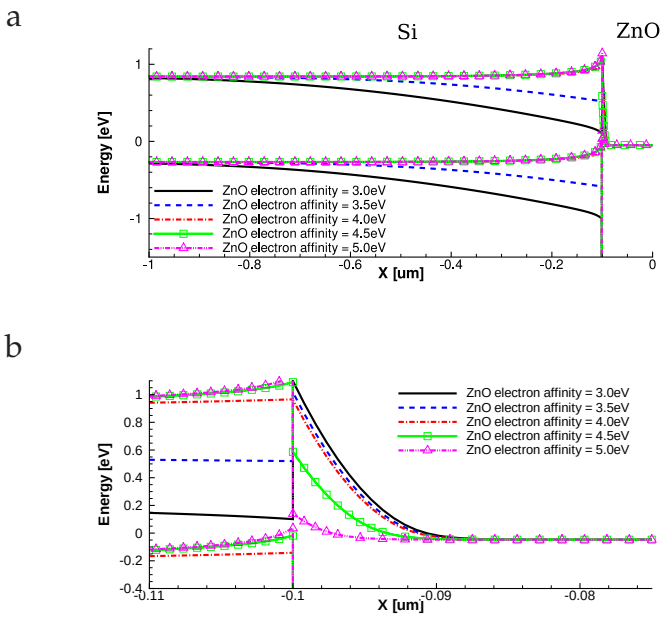

Figure 6.9: Band diagram for $\chi_{ZnO} = 4.5\,\mathrm{eV}$ with an acceptor interface trap density of $10^{13}\,\mathrm{cm}^{-2}$. a) Shows the band bending. b) Shows the energy bands near the junction.

fer now from each other, because large amount of electrons from ZnO are now trapped at the interface rather than transfered to Si. This causes the Fermi-level to be lowered. Thus, the aforementioned "limit" of band bending in Si may not be reached.

Despite the altered IV-shapes, the mechanisms have already been described. A convergence problem was encountered for $\chi_{4.5}$, but it is expected to follow $\chi_{5.0}$ due to the similarity in the lower voltage. Generally, a high acceptor interface trap reduces the rectification of the junction, which can be caused by: 1) increased band-to-band tunneling and 2) lower potential barrier.

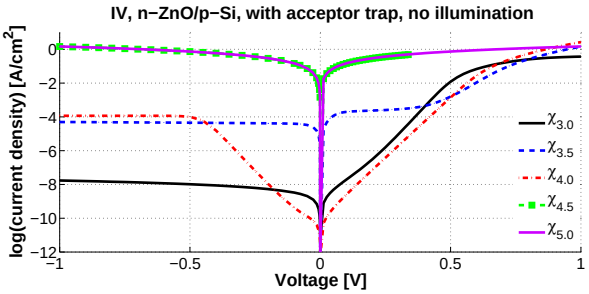

Figure 6.10: IV-curves for n-ZnO/p-Si with acceptor interface trap.

6.2.1.5 n-ZnO/p-Si: Interface trap and illumination

Figure 6.11 shows the IV response of the junction with interface traps under illumination for $\chi_{\leq 4.0}$. Due to the Ohmic nature of $\chi_{\geq 4.5}$ and their large current, no PV effect will appear and a vertical curve along $V = 0$ will be present in the range given in Fig.6.11. Thus, these curves are omitted.

The effect of the disappearence of depletion region is again seen in forward and reverse bias for $\chi_{3.5}$ and $\chi_{4.0}$, respectively (see Fig.6.11). The larger drop with $\chi_{3.5}$ is due to the barrier height and tunneling from ZnO. Comparing simulations without traps, the photocurrent in forward bias is reduced significantly for $\chi_{3.5}$ and $\chi_{4.0}$, while the V_{OC} and I_{SC} are only affected slightly. This results eventually in a decrease in output power.

6.2.1.6 Comparison between n-ZnO and n^+-ZnO

By increasing the n-doping concentration in ZnO from 10^{19} to $10^{20}\,\mathrm{cm}^{-3}$, the band gap energy, the electron affinity and the Fermi-level change by -0.26 eV, +0.11 eV and +0.23 eV, respectively, given by the default physical

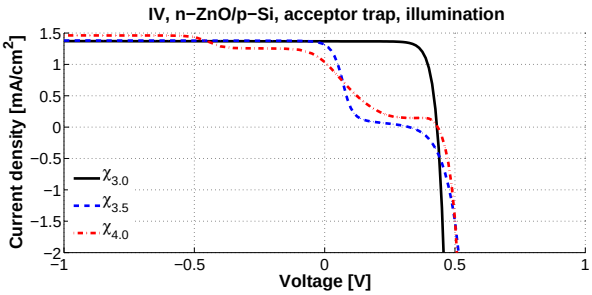

Figure 6.11: IV-characteristics of n-ZnO/p-Si under illumination with acceptor trap.

models. The Fermi-level is effectively increased by $\sim$0.12 eV relative to the lower doped case (see Fig.6.12). These changes are strictly of numerical origin, since the band structure of ZnO is unknown by the program and thus unable to give the real Fermi-level. However, this can provide some physical insight. The depletion width in ZnO is also reduced, as expected

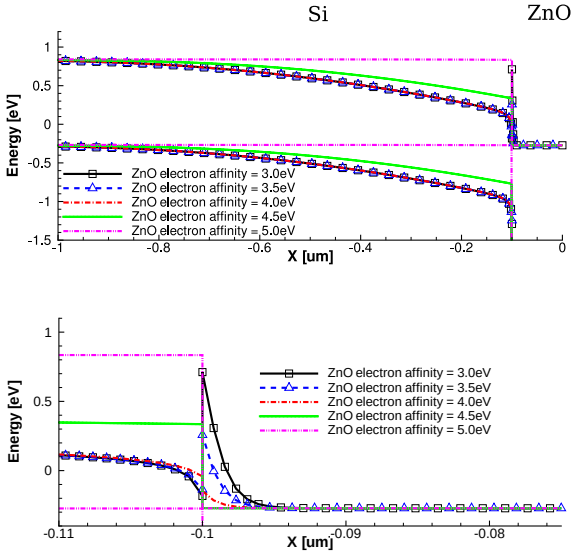

Figure 6.12: Band diagram for n^+-ZnO/p-Si at equilibrium.

by the correlation with the doping concentration in Eq.2.12. However, this narrowing of the depletion width is not expected to contribute for $\chi_{\leq 3.5}$ due to large tunneling.

6.2.1.7 Effects of higher doping on IV-characteristic

Due to numerical errors, simulations were only managed for $\chi_{\leq 4.5}$, and the simulated IV-curves showed no differences between $\chi_{\leq 4.0}$ (not shown), as anticipated. For $\chi_{4.5}$, the observed changes in the IV-curve are affected only by the effective changes in the Fermi-level. Thus, lowering or lifting the electron affinty by 0.12 eV for the low-doped or the highly-doped region, respectively, will provide the same IV-curve, see Fig.6.13.

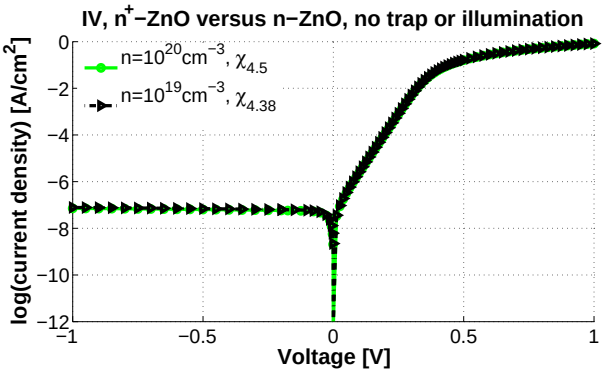

Figure 6.13: Comparison between high and low n-doping concentration of ZnO through the effective change in Fermi-level.

6.2.1.8 Under illumination

Change in V_{OC} is only observed for $\chi_{4.5}$, with a magnitude of 0.12 V corresponding well to the effective shift in the Fermi-level. As $\chi_{\leq 4.0}$ remains completely unchanged (compared to ***n***-ZnO/p-Si), $\chi_{\leq 5.0}$ is only shifted during low forward bias with a value of 0.12 V (see Fig.6.14). Thus, the larger current is believed to be caused by the lowering of potential barrier from CB_{Si} to CB_{ZnO} for the photogenerated electrons near the interface, where the band-to-band tunneling opposes this effect only slightly.

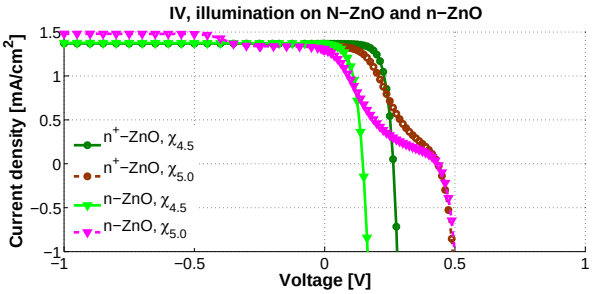

Figure 6.14: Effect on IV-curves for higher emitter concentration, compared with *n*-ZnO/p-Si.

The effects observed with n^+-ZnO can be reproduced by only changing the electron affinity of ZnO. Thus, further simulation with n^+-ZnO was not performed.

6.2.2 n-ZnO/n-Si

6.2.2.1 n-ZnO/n-Si: Band diagram

A structure consisting of n-type ZnO on n-type Si has been simulated, and Fig.6.15 shows the band diagram for this structure. The difference between this band diagram and n-ZnO/***p***-Si can be observed as a lowered CBE and VBE, due to higher Fermi-level. It can also be noted that the bending of CBE_{ZnO} is similar to n-ZnO/***p***-Si.

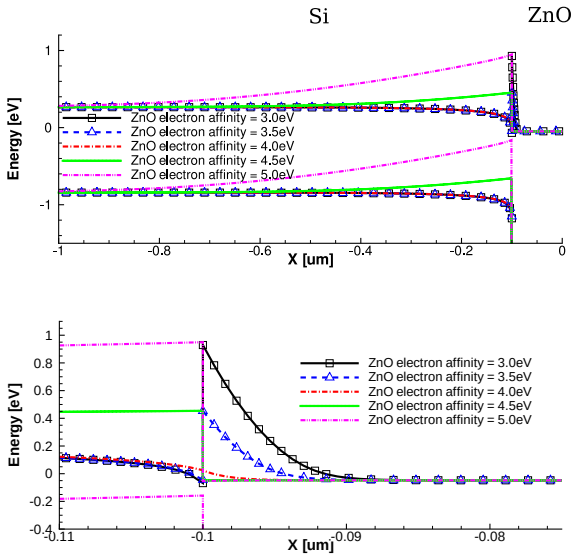

Figure 6.15: Band diagrams for n-ZnO/n-Si.

6.2.2.2 n-ZnO/n-Si: IV-characteristics

In this structure, the rectifying behavior occurs due to ΔE_C, which is controlled by χ_{ZnO}. Due to the low doping concentration in Si, giving rise to the largest depletion width, the thin barrier in ZnO (for $\chi_{ZnO} < \chi_{Si}$) will only contribute to Ohmic behavior. Thus, a rectifying contact occurs if $\chi_{ZnO} > \chi_{Si}$ or if the concentration of acceptor interface states is high. For $\chi_{ZnO} \geq 4.5$ eV, one of the requirements is satisfied, and the IV-curves are shown in Fig.6.16. The missing data for $\chi_{5.0}$ is due to numerical convergence problem.

6.2.2.3 n-ZnO/n-Si: Illumination

A rectifying contact is a requirement in order to achieve PV effects. As shown in Fig.6.16, IV-curves for $\chi_{\leq 4.5}$ exhibit Ohmic or near Ohmic behavior, and simulations under illumination exhibit the same IV-curves as without illumination (not shown). The only good rectifying contact with low leakage current is achieved with $\chi_{5.0}$, but unfortunately, the simulation including illumination ran into nummerical error and no calculations

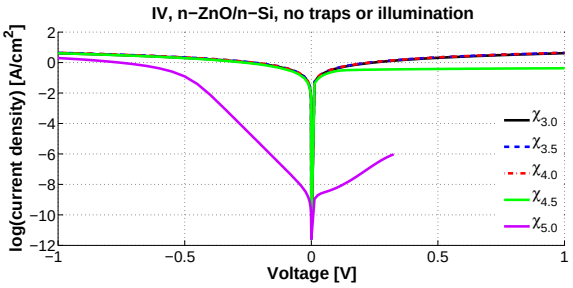

Figure 6.16: IV-curves for n-ZnO/n-Si.

were managed.

In order to obtain any photovoltaic effects, the photogenerated holes from Si are required to cross over to ZnO (in contrast to that in the np case). This can happen by 1) thermal excitation over the extreme barrier to VB_{ZnO} or 2) band-to-band tunneling to CB_{ZnO}, where the latter case is the most probable mechanism. Based on the band diagram for $\chi_{5.0}$, where the photogenerated holes are expected to tunnel to ZnO, a PV effect is also expected.

6.2.2.4 n-ZnO/n-Si: Interface traps

Figure 6.17 shows the band diagram for n-ZnO/n-Si with acceptor traps introduced. The changes from Fig.6.15 are seen by the lowering of Fermi-level for both material at the interface due to an increase of hole concentration. This causes an increase in potential barrier which affects the leakage

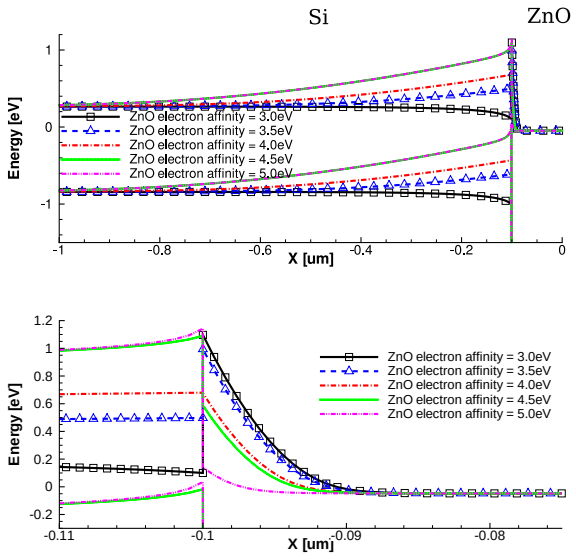

Figure 6.17: Band diagram for n-ZnO/n-Si with acceptor interface trap.

current by reducing its magnitude, shown in Fig.6.18, and a higher rectification can be observed by increasing electron affinity. However, the IV-curve of $\chi_{3.0}$ and $\chi_{5.0}$ are only affected slightly due to the high concentration of either hole or electron before introducing the acceptor trap.

6.2.2.5 n-ZnO/n-Si: Interface traps and illumination

As the criteria for obtaining PV effect are fulfilled for $\chi_{\geq 3.5}$ by gaining a rectification, IV-curves under illumination show photorespons (see Fig.6.19). However, since the leakage current in $\chi_{3.5}$ is already high, the photorespons cannot be seen in this IV-curve. A convergence problem was also

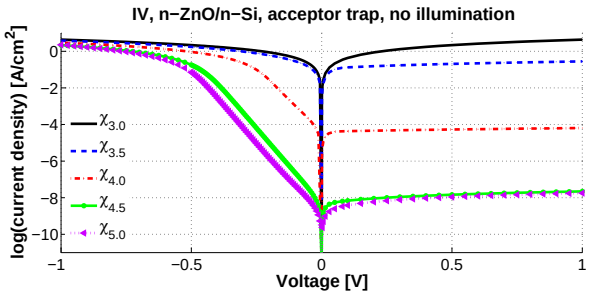

Figure 6.18: IV-curves for n-ZnO/n-Si with acceptor interface trap.

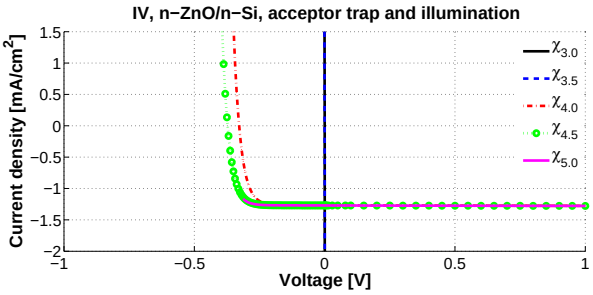

Figure 6.19: IV-curves for n-ZnO/n-Si with interface traps and under illumination.

met in the case for $\chi_{5.0}$ and the program only managed to calculate the current to some extend, but comparing the dark and light currents for curves with $\chi_{\geq 4.5}$, the curve with $\chi_{5.0}$ is expected to be a slightly shifted version of $\chi_{4.5}$. The conversion efficiency for $\chi_{4.5}$ is calculated to be $\sim$12.4% with $V_m \approx -0.31\,\mathrm{V}$ and $I_m \approx -1.16\,\mathrm{mA/cm^2}$.

6.3 Discussion

This section will discuss the simulations in connection with experimental results in the literature. The possible application given by the simulated results will also be discussed.

n-ZnO/n-Si junction

As shown in the literature, high PV efficiency can be obtained through an nn-junction of ZnO and Si. Simulations performed in this work have shown the possible carrier transport in such a junction which provides the PV effect. However, a high electron affinity and high acceptor interface trap density, leading to large rectification, are required. Such large rectification has not been achieved experimentally, in the few reported work on this heterostructure. Comparing the IV-curves from the literature and the simulation conditions for nn-junction in the present work, where PV effects are observed, it suggests that χ_{ZnO} is above 4 eV. This assumes that the electron affinity does not differ significantly between bulk and surface.

n-ZnO/p-Si junction

The experimental IV-curve for an illuminated np-junction, shown in Fig.3.7, has not been reproduced by the simulations. All np-models gave a reverse current different from the ones described in the literature. In fact, a PV effect has been a fairly easy task to simulate, since the seperation of EHP does not require holes surmounting a large barrier to ZnO. The photogenerated electrons, on the other hand, experience nearly no barrier on the way to ZnO. Thus, to simulate the IV-curves for n-ZnO/p-Si in the literature, additional mechanisms are required to reduce the transport of photogenerated electrons to ZnO. In a real structure of ZnO on Si, a native oxide layer of Si exists at the interface. This suggests that the oxide layer and its interface defects are causing the reported IV-curves in the literature.

ZnO and its application to solar cells

Although the exact electron affinity of ZnO is not known, the present work has provided a map on how ZnO can act in an ideal case in the heterostructure of ZnO/Si. This sets the upper limit on the performance in applications such as solar cells. The proposed usages of ZnO in the solar cells are the emitter, ARC and TCO. Based on the simulated results, the suitability of ZnO for will be discussed.

ZnO as an emitter

To act as an emitter, a large rectification is required to seperate the photogenerated EHP. This was achieved in both type of junction, where the highest efficiency was obtained through n-ZnO/n-Si (with high χ_{ZnO} or aided by interface trap) and n-ZnO/p-Si junction (with $\chi_{\leq 4.0}$). Under illumination using light at 2 eV and power of 2.9 mW/cm^2, these cells reached a conversion efficiency of $\sim$13-16%, having $V_m \approx 0.36$ V and $I_m \approx 0.13$ mA/cm^2. This illustrates the possibility for ZnO to act as an emitter.

ZnO as a TCO/ARC

Even though the ZnO layer may not provide a rectifying junction with n-Si, as achieved in a wide range of electron affinity of ZnO ($\chi_{\leq 4.5}$ without interface trap) in the nn-junction, its Ohmic behavior can act as TCO on top of an n$^+$-Si emitter. This construction can reduce the amount of metal front contact fingers which block incident light, and thus improving the efficiency of existing Si-based solar cells. The combination of TCO and ARC also removes the requirement of metal contact directly into the emitter. This avoids the step of firing-through the ARC to reach the emitter, which can induce detrimental defects.

Chapter 7

Summary

7.1 Conclusions

A simulation model of the electrical transport properties of ZnO has been developed based on the findings in the literature and experimental characterization of Pd Schottky contacts. Using this model, simulation of ZnO/Si heterostructure was investigated.

Simulations of Pd Schottky contacts on ZnO were performed in connection with the developement of the model, and the simulated IV-curves showed large dependence on the interface trap concentration when tunneling was applied. A trap density between $4.5 \times 10^{12} - 8.0 \times 10^{12}\,\mathrm{cm}^{-2}$ was shown to describe reasonably well the leakage currents for the experimental IV-curves with the highest rectification.

The heterostructure of ZnO on Si was investigated numerically through a wide range of value for ZnO electron affinity (3-5 eV). This provided a general picture on how the combination of Si with materials within the selected range may act, such as ZnO and ITO, including the presence of interface trap and illumination. For nn-junctions, it was found that photovoltaic effects could only be generated for high χ_{ZnO} ($>\chi_{Si}$) or with high concentration of acceptor interface traps. As for the effect of acceptor interface traps on the n-ZnO/p-Si heterojunction, it was observed that the rectification decreased with increasing trap density, causing a lower PV effect. Based on the findings in the literature, where n-ZnO/n-Si hetero-

junctions are more often reported with a PV effect than n-ZnO/p-Si junction and in addition with a much higher efficiency, it is believed that the electron affinity of ZnO is higher than that of Si and that an interfacial layer of electron trap is present.

7.2 Suggestions for future work

In-diffusion of hydrogen

The time-degradation of the Pd Schottky contact made the electrical measurements challenging in the sense that all nescessary data were needed to be aquired within a few days after deposition for the heat treated samples. Remeasurements became, thus, less reliable due to the change in the contact quality. Hydrogen indiffusion, which can increase the interface n-doping and tunneling, has been suggested as a cause of the time degradation in the literature [47]. This hypothesis may be tested by performing electrical measurement before and after an annealing in hydrogen atmosphere.

Polishing induced defects

The contact degradation rate was qualitatively observed to be higher in polished samples. PAS measurements in literature [65] have shown generation of defects by polishing, which can be removed by heat treatment at around 1000°C. Whether the creation of polishing defects can enhance the degradation rate will be interesting to know. A post-flash-annealing may provide the condition to remove the induced defects. Thus, two samples from one wafer could be heat treated (at, for instance, 1200°C) and polished, where one sample undergoes a flash-annealing before contact deposition. Several electrical measurements on the same contact should then be performed as a function of time.

Deep levels

The DLTS spectra after 1200°C and 1500°C treatment showed different behavior at high temperature (>300K) irrespective of the wafers. The evolution of the spectra suggests a defect level at higher temperature (see Fig.5.6). Since a shift of DLTS peak position to higher temperature can be caused by a smaller capture cross section, the defect levels might not necessarily be deeper than the ones measured. It will be interesting to see whether these defects at higher temperature coincide with the intrinsic defects calculated by DFT. ADSPEC measurement will also be helpful to collect the information about these defects for high resistive wafers at elevated temperatures.

Pd Schottky contact simulation model

One observed limitation of the Pd Schottky model was the high capacitance gradient at low revers bias. This was attributed to a highly n-doped interface layer, which was required in order to achieve a significant tunneling effect. However, this layer also caused a very narrow depletion layer. A study which includes an electrical active impurity with a non-uniform concentration-versus-depth profile might be interesting to see how it affects the electrical properties of the Schottky contact.

ZnO/Si heterstructure simulation model

The ZnO/Si model implemented in this work had an abrupt transition between ZnO and Si. In reality, a native oxide layer of 1.0-1.5 nm is formed on Si, which can passivate the interface and reduce the defect concentration. However, tunneling of charge carrier through the oxide layer may differ between electrons and holes. This can favor the PV effect for either the isotype (nn) or anisotype (np) heterojunction. More efforts are then required in tuning the tunneling parameters, oxide thickness and the defect concentration between Si and the interfacial oxide.

Appendix A

Derivations

A.1 Trap level and capture cross section

Thermodynamically, the electron emission rate is expressed as

$$e_n = v_{th}\sigma N_C exp\left(\frac{-\Delta G_n}{kT}\right) \quad , \Delta G_n = \Delta H_n - T\Delta S_n \tag{A.1}$$

where G_n is the Gibbs free energy, H_n is the entalphy and S_n is the entropy. It should be noted that the energy difference between CBE and trap level ($E_C - E_T$) is given by *both* ΔH_n and ΔS_n. However, when the difference is written in this form, the gradient in the Arrhenius plot no longer contains both the quantities (see Eq.A.2).

$$ln\left(\frac{e_n}{T^2}\right) = ln\left(\left[\frac{8\pi^{3/2}m^*k^2}{h^3}\right]\cdot\sigma_n\, exp\left(\frac{\Delta S_n}{k}\right)\right) - \left(\frac{\Delta H_n}{k}\right)\frac{1}{T} \tag{A.2}$$

Moreover, the constant term is also affected by the entropy which disturbs the extraction of the capture cross section. Thus, in reality, neither energy level of the trap or the capture cross section can be evaluated from the Arrhenius plot without knowing the change in entropy, which in most cases is unknown. However, if the entropy change is negligibly small, the enthalpy will be equal to the Gibbs free energy, i.e. the trap energy level.

A.2 Diode equation

A diffusion process is governed by a gradient in a concentration. The gradient at the edge of the depletion zone is achived through thermal excitation of carriers overcoming the potential barrier and modified by the external voltage. Under equilibrium, the ratio of the hole concentration at each side of the depletion zone is

$$\frac{p_p}{p_n} = exp\left(\frac{qV_0}{kT}\right) \tag{A.3}$$

where the subscripts (n and p) indicate the type of material. While under external voltage, it becomes

$$\frac{p(-x_{p0})}{p(x_{n0})} = exp\left[\frac{q(V_0 - V)}{kT}\right] \tag{A.4}$$

If the external voltage is small, such that

$$\frac{p(-x_{p0})}{p_p} \approx 1 \tag{A.5}$$

the excess minority carrier can be expressed, using Eq.A.3 and Eq.A.4, as

$$\Delta p_n = p(x_{n0}) - p_n = p_n\left[exp\left(\frac{qV}{kT}\right) - 1\right] \tag{A.6}$$

These excess carriers will, due to concentration gradient, diffuse away from the depletion zone and into the bulk material. Under new sets of coordinate (See Fig.A.1)[1], the excess concentration at any given point in the bulk material is in Eq.A.7.

$$\delta p(x_n) = \Delta p_n exp\left(\frac{-x_n}{L_p}\right) = p_n\left[exp\left(\frac{qV}{kT}\right) - 1\right] exp\left(\frac{-x_n}{L_p}\right) \tag{A.7}$$

where L_p is the diffusion length for holes. The diffusion current density, more specifically defined, is

$$J_p(x_n) = -qD_p\frac{d\,\delta p(x_n)}{dx_n} = q\frac{D_p}{L_p}\delta p(x_n) \tag{A.8}$$

[1] To simplify the mathematics.

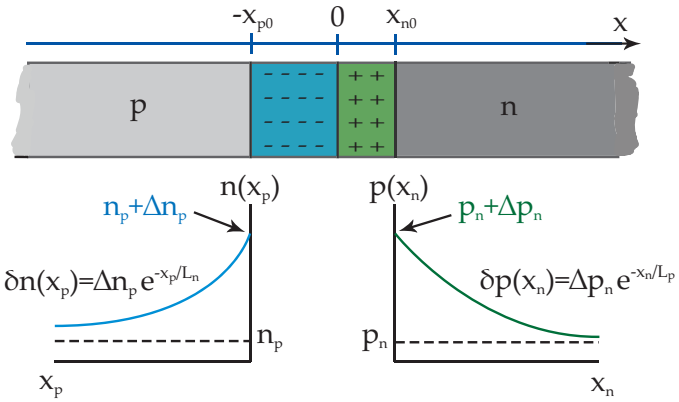

Figure A.1: Band alignment between a metal and an n-type semiconductor.

The electron diffusion current density, can be achived by interchanging p with n and q with -q. Considering the definition of the new coordinate system and combining Eq.A.7 and E.A.8, the total diffusion current at the edge of the depletion zone becomes

$$J = J_p(x_n = 0) - J_n(x_p = 0) = q\left(\frac{D_p}{L_p}p_n + \frac{D_n}{L_n}n_p\right)\left[exp\left(\frac{qV}{kT}\right) - 1\right] \tag{A.9}$$

which is known as the ideal *diode equation*

$$J = J_0\left[exp\left(\frac{qV}{kT}\right) - 1\right] \tag{A.10}$$

Appendix B

Synopsys TCAD files

B.1 Sentaurus Structure Editor: Example command file

```
;;#A pn-junction consisting of n-ZnO/p-Si is built in this example.
;;;Input variables are defined by @....@

(sdegeo:set-default-boolean "ABA") (sdegeo:set-default-boolean "ABA")
(define width 0.1)
(define height (* width 0.67))
(define Ndoping @NDoping@)
(define Pdoping @PDoping@)
;----------Structure------------
;;#Choose and position the materials
(sdegeo:create-rectangle (position 0 0 0) (position (* width 0.5) height 0)
  "Silicon" "p-side")
(sdegeo:create-rectangle (position (* width 0.5) 0 0) (position width height 0)
  "ZnOHydrothermal" "n-side")
;----------Doping---------------
;;#Assign doping type and concentration to the regions
(sdedr:define-constant-profile "Const.N" "PhosphorusActiveConcentration" Ndoping)
(sdedr:define-constant-profile-region "PlaceC.N" "Const.N" "n-side")
(sdedr:define-constant-profile "Const.P" "BoronActiveConcentration" Pdoping)
```

```
(sdedr:define-constant-profile-region "PlaceC.P" "Const.P" "p-side")
;----------Contact-------------
;;#Define contacts to edges
(sdegeo:define-contact-set "ContactP" 4 (color:rgb 1 0 1) "##")
(sdegeo:define-2d-contact (find-edge-id (position 0 (/ height 2) 0))
  "ContactP")
(sdegeo:define-contact-set "ContactN" 4 (color:rgb 0 1 0) "##")
(sdegeo:define-2d-contact (find-edge-id (position width (/ height 2) 0))
  "ContactN")
;--------Refinement and mesh------------
;;#Define and place a desirable mesh
(sdedr:define-refinement-window "RefWinAll" "Rectangle"
  (position 0 0 0) (position width height 0) )
(sdedr:define-refinement-window "RefWinCP" "Rectangle"
  (position (* width 0.90) 0 0) (position 1 height 0) )
(sdedr:define-refinement-window "RefWinCN" "Rectangle"
  (position 0 0 0) (position (* width 0.10) height 0) )

(sdedr:define-refinement-size "RefDefAll" (/ width 200) (/ height 1)
  (/ width 500) (/ height 1) )
(sdedr:define-refinement-placement "PlaceRFAll" "RefDefAll" "RefWinAll")
(sdedr:define-refinement-size "RefDefCP" (/ width 200) (/ height 1)
  (/ width 500) (/ height 1) )
(sdedr:define-refinement-placement "PlaceRFDep" "RefDefDep" "RefWinDep")
(sdedr:define-refinement-size "RefDefCN" (/ width 200) (/ height 1)
  (/ width 500) (/ height 1) )
(sdedr:define-refinement-placement "PlaceRFCN" "RefDefCN" "RefWinCN")
;-----------save and build--------------------
(sdeio:save-tdr-bnd (get-body-list) "@tdrboundary/o@")
(sdedr:write-cmd-file "@commands/o@")
(system:command "mesh -F tdr n@node@_msh")
```

B.2 Sentaurus Device: Example command file

```
###Simulation conditions in terms of physical model, mathematical
###interpretations and ramping parameters are spesified for the
###pn-junction

###Specifies the name of input and output files
File {
 Grid  = "@tdr@"
 Param = "@parameter@"
 Current = "@plot@"
 Plot    = "@tdrdat@"
 Output  = "@log@"
}

###Initial condition for the electrodes
Electrode {
 {Name = "ContactN" Voltage = 0.0}
 {Name = "ContactP" Voltage = 0.0}
}

###Physical considerations, such as tunneling and
###band gap narrowing models.
Physics {
 Mobility (DopingDependence HighFieldsat Enormal)
 EffectiveIntrinsicDensity( OldSlotboom )
 Temperature = 300
 Fermi

 Recombination ( Auger SRH(DopingDep) )
}

Physics(RegionInterface="n-side/p-side") {
 Recombination(
```

```
  eBarrierTunneling(Band2Band TwoBand Bandgap)
  hBarrierTunneling(Band2Band TwoBand Bandgap)
  SurfaceSRH
 )
}

###Desirable output physical parameters
Plot {
 eDensity  hDensity  eCurrent  eQuasiFermi hQuasiFermi
 eMobility  hMobility  eLifeTime hLifeTime
 eTrappedCharge hTrappedCharge
 "hRelativeEffectiveMass" "eRelativeEffectiveMass"
 "hEffectiveStateDensity" "eEffectiveStateDensity"
 hGradQuasiFermi eGradQuasiFermi eBarrierTunneling hBarrierTunneling
 Potential  SpaceCharge  ElectricField Doping
 DonorConcentration  AcceptorConcentration
 BandGapNarrowing EffectiveBandGap
 AugerRecombination SRHRecombination TotalRecombination
 Band2Band "BuiltinPotential" TotalTrapConcentration
 RadiativeRecombination EffectiveBandGap EffectiveIntrinsicDensity
 ConductionBandEnergy ValenceBandEnergy
 Bandgap ElectronAffinity  EquilibriumPotential Nonlocal
}

###Mathematical considerations, such as convergence
###criteria and solve method
Math {
 Extrapolate
 RelErrControl
 DirectCurrent
 Extendedprecision
 NotDamped=40
 Iterations=20
}
```

```
###Additional specifications for the tunneling method
Math (RegionInterface="n-side/p-side") {
 Nonlocal(Length=15e-7)
 Digits(NonLocal)=4
 EnergyResolution(NonLocal)=0.0001
}

###Solves the Poissons equation coupled with the continuity equations
###for various potential at ConctactP until voltage @Voltage@ is reached
Solve {
 Poisson
 Coupled{Poisson Electron Hole}

 Quasistationary
  (Goal {Name = "ContactP" Voltage= @Voltage@}
   InitialStep = 0.001 Maxstep=0.03 Minstep=0.000002
  ) {Coupled {poisson electron hole}
}
```

Bibliography

[1] Victoria Anne Coleman. Processing and characterization of ZnO for device applications. Ph.D. thesis, The Australian National University, 2006.

[2] Ü. Özgür, Ya. I. Alivov, C. Liu, A. Teke, M. A. Reshchikov, S. Dogan, and V. Avrutin. A comprehensive review of ZnO materials and devices. *Journal of applied physics*, 98(041301), 2005.

[3] N. Ashkenov, N. Mbenkum, C. Bundesmann, V. Riede, M. Lorenz, D. Spemann, E. M. Kaidashev, A. Kasic, M. Schubert, M. Grundmann, G. Wagner, H. Neumann, V. Darakchieva, H. Arwin, and B. Monemar. Infrared dielctric functions and phonon modes of high-quality ZnO films. *Journal of applied physics*, 93(1), 2002.

[4] Charles Kittel. *Introduction to Solid State Physics, 8th ed.* Wiley, 2005.

[5] M. R. A. Shegelski. The chemical potential of an ideal intrinsic semiconductor. *American journal of physics*, 72(5), 2004.

[6] Ben G. Streetman and Sanjay Kumar Banerjee. *Solid state electronic devices, 6th ed.* Pearson Prentice Hall, 2000.

[7] P. Biljanovic and T. Suligoj. Thermionic emission process in carrier transport in pn homojunctions. *10th Mediterranean electrotechnical conference*, 1, 2000.

[8] A. M. Goodmann. Metal-semiconductor barrier height measurement by the differential capacitance method - one carrier system. *Journal of applied physics*, 34(2), 1962.

[9] D. K. Schroder. *Semiconductor material and device characterization, 1st ed.* Wiley-Interscience, 1990.

[10] J. Emsley. *Nature's building blocks*. Oxford University Press, 2003.

[11] F. C. Porter. *Zinc handbook: Properties, processing, and use in design*. Marcel Dekker, 1991.

[12] A. Weidenkaff, A. W. Reller, A. Wokaun, and A. Steinfeld. Thermogravimetric analysis of the ZnO/Zn water splitting cycle. *Thermochimica Acta*, 359:69–75, 2000.

[13] R. Schifano, E. V. Monakhov, L. Vines, B. G. svensson, W. Mtangi, and F. D. Auret. Role of lithium and aluminium on the electrical properties of hydrothermally grown ZnO. *unpublished*, 2008.

[14] D. C. Look. Unusual electrical properties of hydrothermally grown ZnO. *Superlattices and microstructures*, 42:284–289, 2007.

[15] S. J. Pearton, D. P. Norton, K. Ip, Y. W. Heo, and T. Steiner. Recent progress in processing and properties of ZnO. *Progress in Material Science*, 50:293–340, 2005.

[16] C. Jagadish and S. J. Pearton. *Zinc oxide bulk, thin films and nanostructures*. Elsevier, 2006.

[17] S. M. Sze. *Physics of semiconductor physics, 2nd ed.* Wiley-Interscience, 1981.

[18] O. F. Sankey A. Kobayashi and J. D. Dow. Deep energy levels of defects in the wurtzite semiconductors AIN, CdS, CdSe, ZnS, and ZnO. *Physical review b*, 28:946, 1983.

[19] S. Majumdar, S. Chattopadhyay, and P. Banerji. Electrical characterization of p-ZnO/p-Si heterojunction. *Applied surface science*, 255:6141–6144, 2009.

[20] Y. F. Gua, X. M. Lia, J. L. Zhaoa, W. D. Yua, X. D. Gaoa, and C. Yanga. Visible-blind ultra-violet detector based on n-ZnO/p-Si heterojunction fabricated by plasma-assisted pulsed laser deposition. *Solid state communications*, 143:421–424, 2007.

[21] D. W. Ma, Z. Z. Ye, and L. L. Chen. Dependence of structural and optical properties of $Zn_{1-x}Cd_xO$ films on the Cd composition. *Physica status solidi a*, 201(13), 2004.

[22] S. Choopun, R. D. Vispute, W. Yang, R. P. Sharma, T Venkatesan, and H. Shen. Realization of bang gap above 5.0ev in meta stable cubic-phase $Mg_xZn_{1-x}o$ alloy films. *Applied physics letter*, 80:1529, 2002.

[23] E. V. Kortunova, N. G. Nikolaeva, P. P. Chvanski, V. V. Maltsev, E. A. Volkova, E. V. Koporulina, N. I. Leonyuk, and T. F. Kuech. Hydrothermal synthesis of improved ZnO crystals for epitaxial growth of GaN thin films. *Journal of materials science*, 43:2336–2341, 2007.

[24] K. Maeda, M. Sato, I. Niikura, and T. Fukuda. Growth of 2 inch ZnO bulk single crystal by the hydrothermal method. *Semiconductor science and technology*, 20:S49–S54, 2005.

[25] T. Maqsood. Hydrothermal ZnO; Mastering of lithium content and formation of palladium Schottky diodes. Master thesis, University of Oslo (UiO), Norway, 2008.

[26] S. Seto, S. Yamada, K. Suzuki, and K. Yoshino. Emissions from deep levels in hydrothermal grown ZnO substrates. *Journal of the Korean Physical Society*, 53(5):2959–2962, 2008.

[27] D. C. Look, D. C. Reynolds, J. R. Sizelove, R. L. Jones, C. W. Litton, G. Cantwell, and W. C. Harsch. Electrical properties of bulk ZnO. *Solid state communications*, 105(6), 1998.

[28] J. Nause and B Nemeth. Pressurized melt growth of ZnO boules. *Semiconductor Science Technology*, 20:45–48, 2005.

[29] A. Janotti and C. G. Van de Walle. Native point defects in ZnO. *Physics review B*, 76(165202), 2007.

[30] H. von Wenckstern, H. Schmidt, M. Grundmann, M. W. Allen, P. Miller, R. J. Reeves, and S. M. Durbin. Defects in hydrothermally grown ZnO. *Applied physics letters*, 91(022913), 2007.

[31] F. D. Auret, S. A. Goodmann, M. J. Legodi, W. E. Meyer, and D. C. Look. Electrical characterization of vapor-phase-grown single-crystal ZnO. *Applied physics letters*, 80(8), 2002.

[32] Q. L. u, C. K. Cheung, C. C. Ling, A. M. C. Ng, A. B. Djurisic, L. W. Lu, X. D. Chen, S. Fung, C. D. Beling, and H. C. Ong. Au/n-ZnO rectifying contact fabricated with hydrogen peroxide pretreatment. *Journal of applied physics*, 103(093706), 2008.

[33] T. Frank, G. Pensl, R. Tena-Zaera, J Zúñiga-Pérez, C. Martínez-Tomás, V. Muñoz-Sanjosé, T. Ohshima, H. Itoh, D. Hofmann, D. Pfisterer, J. Sann, and B. Meyer. Energitically deep defect centers in vapor-phase grown zinc oxide. *Applied physics A*, 88:141–147, 2007.

[34] T. Minami, H. Sato, and H. Nanto. Group III doped zinc oxide thin films prepared by rf magnetron sputtering. *Japanese journal of applied physics*, 24(10):L781–L784, 1985.

[35] Seung Yeop Myong, Seung Jae Baik, Chang Hyun Lee, Woo Young Cho, and Koeng Su Lim. Extremely transparent and conductive ZnO:Al thin films prepared by photo-assisted metalorganic chemical vapor deposition (photo-MOCVD) using $AlCl_3 \cdot (6H_2O)$ as new doping material. *Japan journal of applied physics*, 36(L1078), 1997.

[36] B. M. Ataev, A. M. Bagamadova, A. M. Djabrailov, V. V. Mamedov, and R. A. Rabadanov. Highly conductive and transparent Ga-doped epitaxial ZnO films on sapphire by CVD. *Thin solid films*, 260:19–20, 1995.

[37] C. G. van de Walle. Hydrogen as a cause of doping in zinc oxide. *Physical review letters*, 85(5), 2000.

[38] C. G. van de Walle. Hydrogen as a shallow center in semiconductors and oxides. *Physica status solidi (b)*, 235(1):89–95, 2003.

[39] U. Wahl, E. Rita, J. G. Correia, A. C. Marques, E. Alves, and J. C. Soares. Direct evidence for As as a Zn-site impurity in ZnO. *Physical review letters*, 95(215503), 2005.

[40] Hong Seong Kang, Gun Hee Kim, Dong Lim Kim, Byung Du Ahn Hyun Woo Chang, and Sang Yeol Lee. Investigation on the p-type formation mechanism of arsenic doped p-type ZnO thin film. *Applied Physics Letters*, 89(18):181103, 2006.

[41] C A Mead. Surface barrier on ZnSe and ZnO. *Physics Letters*, 18(218), 1965.

[42] A. Y. Polyakov, N. B. Smirnov, E. A. Kozhukhova, V. I. Vdovin, K. Ip, Y. W. Heo, D. P. Norton, and S. J. Pearton. Electrical characteristics of Au and Ag Schottky contacts on n-ZnO. *Applied physics letters*, 83(8), 2003.

[43] B. J. Coppa, C. C. Fulton, S. M. Kiesel, R. F. Davis, C. Pandarinath, J. E. Burnette, R. J. Nemanich, and D. J. Smith. Structural, microstructural, and electrical properties of gold films and Schottky contacts on remote plasma-cleaned, n-type ZnO {0001} surfaces. *Journal of Applied Physics*, 97(103517), 2005.

[44] R. Schifano, E. V. Monakhov, U. Grossner, and B. G. Svensson. Electrical characteristics of palladium Schottky contacts to hydrogenperoxide trated hydrothermally ZnO. *Applied Physics Letters*, 91(193507), 2006.

[45] K. Ip, B. P. Gila, A. H. Onstine, E. S. Lambers, Y. W. Heo, K. H. Baik, D. P. Norton, S. J. Pearton, S. Kim, J. R. LaRoche, and F. Ren. Effect of ozone cleaning on Pt/Au and W/Pt/Au Schottky contacts to n-type ZnO. *Applied surface science*, 236:387–393, 2004.

[46] M. W. Allen, M. M. Alkaisi, and S. M. Durbin. Metal Schottky diodes on Zn-polar and O-polar bulk ZnO. *Applied Physics Letters*, 89(103520), 2006.

[47] Y. Dong, D-Q. Fang, D. C. Look, G. Cantwell, J. Zhang, J. J. Song, and L. J. Brillson. Zn- and O-face polarity effects at ZnO surfaces and metal interfaces. *Applied physics letters*, 93(072111), 2008.

[48] C. C. Ling, C. K. Cheung, Q. L. Gu, X. M. Dai, S. J. Xu, C.Y Zhu, J. M. Luoo, C. Y. Zhu, K. H. Tam, A. B. Djurisic, C. D. Beling, S. Fung, L. W. Lu, G. Brauer, W. Anwand, W. Skorupa, and H. C. Ong. Defect study in ZnO related structures - A multi-spectroscopic approach. *Applied surface science*, 255, 2008.

[49] M. W. Allen, S. M. Durbin, and J. B. Metson. Silver oxide Schottky contacts on n-type ZnO. *Applied Physics Letters*, 91(053512), 2007.

[50] M. W. Allen and S. M. Durbin. Influence of oxygen vacancies on Schottky contacts to ZnO. *Applied Physics Letters*, 92(122110), 2008.

[51] H. Kobayashi, H. Mori, T. Ishida, and Y. Nakato. Zinc oxide/n-Si junction solar cells produced by spray-pyrolysis method. *Journal of applied physics*, 77:3, 1994.

[52] D. A. Melnick. Zinc oxide photoconduction, an oxygen adsorption process. *Journal of chemical physics*, 26(5), 1957.

[53] D. Song, A. G. Aberle, and J. Xia. Optimisation of ZnO:Al films by change of sputter gas pressure for solar cell application. *Applied surface science*, 195:291–296, 2002.

[54] D. Song, P. Widenborg, W. Chin, and A. G. Aberle. Investigatin of lateral parameter variations of Al-doped zinc oxide films prepared on glass substrates by rf magnetron sputtering. *Solar energy material and solar cells*, 73:1–20, 2002.

[55] D. G. Baik and S. M. Cho. Application of sol-gel derived films for ZnO/n-Si junction solar cells. *Thin sold films*, 354:227–231, 1999.

[56] J. Y. Lee, Y. S. Choi, J. H. Kim, M. O. Park, and S. Im. Optimizing n-ZnO/p-Si heterojunctions for photodiode applications. *Thin solid films*, 403-404:553–557, 2002.

[57] W. Zhang, Q. Meng, B. Lin, and Z. Fu. Influence of growth conditions on photovoltaic effect of ZnO/Si heterojunction. *Solar energy materials and solar cells*, 92:949–952, 2008.

[58] Synopsys. Sentaurus structure editor manual, 2007.

[59] Synopsys. Sentaurus device manual, 2007.

[60] R.E. Bank and D.J. Rose. Global approximate Newton methods. *Numerische Mathematik*, 37:279–295, 1981.

[61] M. Mikelsen. Thermal evolution of irratiation-induced defects in silicon and silicon carbide. Ph.D. thesis, University of Oslo (UiO), Norway, 2007.

[62] SPC Goodwill. Single crystal hydrothermally grown ZnO data-sheet. http://www.spcgoodwill.com/catalog_f.html, 2009.

[63] N Keskitalo. Irradiation induced defects for lifetime control in silicon. Ph.D. thesis, Uppsala University, Sweden, 1997.

[64] M. Ieong, P. M. Solomon, and S. E. Laux. Comparison of raised and schottky source/drain MOSFETs using a novel tunneling contact model. *IEDM Technical Digest*, 1998.

[65] F. A. Selim, M. H. Weber, D. Solodovnikov, and K. G. Lynn. Nature of native defects in ZnO. *Physical review letters*, 99(085502), 2007.